2015

A broadband bistable piezoelectric cantilever-based vibration energy harvester with nonlinear high power extraction

Kanishka Aman Singh
Iowa State University

Recommended Citation

Singh, Kanishka Aman, "A broadband bistable piezoelectric cantilever-based vibration energy harvester with nonlinear high power extraction" (2015). *Graduate Theses and Dissertations*. 14871.
https://lib.dr.iastate.edu/etd/14871

A broadband bistable piezoelectric cantilever-based vibration energy harvester with nonlinear high power extraction

by

Kanishka Aman Singh

A dissertation submitted to the graduate faculty

in partial fulfillment of the requirements for the degree of

DOCTOR OF PHILOSOPHY

Major: Electrical Engineering

Program of Study Committee:
Ratnesh Kumar, Major Professor
Robert J. Weber
Liang Dong
Ayman Fayed
Michael Castellano

Iowa State University

Ames, Iowa

2015

DEDICATION

This work is dedicated to my parents, *Anil Kumar Aman* and *Chanda Aman Singh*, my sisters, *Sneha* and *Pallavi*, and my love, *Rohini*.

TABLE OF CONTENTS

LIST OF FIGURES

LIST OF TABLES

ACKNOWLEDGMENTS

This work has been made possible through the support of a number of people. My first note of thanks goes to my advisors, *Dr. Ratnesh Kumar* and *Dr. Robert J. Weber*, whose help and guidance, every step of the way, were indispensable in the completion of this work. Their advice, suggestions, and patience challenged and encouraged me to learn and to explore.

I would also like to thank my committee members, *Dr. Liang Dong*, *Dr. Ayman Fayed*, and *Dr. Michael Castellano*, for all their help; the discussions I had with each one of them challenged me to think out of the box and broaden my perspective. The course I took with *Dr. Dong* on MEMS helped me expand my knowledge, and the course on power management with *Dr. Fayed* was invaluable for this work.

I would like to thank all the professors whose courses I have used as stepping stones to complete this work. I would also like to express my gratitude to all the faculty and staff at Iowa State University, especially in the Department of Electrical and Computer Engineering and in the Graduate College, for making my time at the University a smooth ride. *Leland Harker* deserves a special mention here for helping in building the harvester prototype.

I am thankful to my colleagues in the lab; it has been an extremely enjoyable experience working and playing with them, and I was able to learn a lot from them. I am also grateful to all my friends in Ames, IA and Munster, IN, whose cheerful company made for some indelible memories. I would especially like to mention *Sneha* and *Arko* for four extremely memorable years of my life, and bearing with me for those four years.

I would like to mention my parents, *Anil Kumar Aman* and *Chanda Aman Singh*, my sisters, *Sneha* and *Pallavi*, and my family in Munster, *Kumar Ranjan Chatterjee*, *Debahuti Chatterjee*, and *Rohan Chatterjee*, for all the endless love and affection they have showered on me throughout. It would have been difficult to get to where I am without their encouragement and support.

Finally, I would like to mention my wife, the love of my life, the one force which keeps pushing me to take that one more step when I feel I have reached the end. *Rohini, for you, the world.*

ABSTRACT

This work presents a nonlinear vibration energy harvester, which combines a nonlinear bistable broadband piezoelectric cantilever used to transduce ambient vibration energy, with synchronized capture for efficient harvesting over broadband sources. An accurate model of the bistable transducer, that augments the Butterworth van Dyke piezoelectric model to capture the external magnetic force added as a bias to the external vibrations, is presented. Its validity has been demonstrated through physical implementation and experimental validation against simulation of the mathematical model. For efficient extraction of the transduced energy, nonlinear extraction circuits, namely synchronous charge extraction (SCE) and parallel synchronized switch harvesting on inductor (SSHI), are employed. The switching in these circuits is implemented using a fully self-propelled, low-power electronic breaker circuit, capable of detecting extrema in the waveform to perform switching. Both simulated and experimental power outputs from the bistable harvester have been presented, with the SCE and parallel-SSHI providing average outputs with more than one-hundred (100) fold increase over the harvested power reported in literature for the same input, and further, even more significant gains are observed for broadband excitations.

For the above mentioned harvester, bistability is introduced through the use of two repelling magnets, one mounted on the cantilever tip and the other at a fixed location opposite it. Excitations that can overcome the repulsive magnetic force cause the cantilever to snap between its two equilibrium states, increasing amplitude and velocity of vibration, resulting in higher power outputs. This improved performance is observed whenever the cantilever operates in the bistable mode. Lower-amplitude excitations are unable to overcome the repulsive force, causing the cantilever to vibrate around one of its equilibrium states, and with smaller amplitudes in the presence of the opposing repulsion. To circumvent this issue, the second part of the work presents a completely mechanical way of increasing the range of excitation amplitudes over which the system remains bistable, by spring-loading the previously fixed-positioned magnet, and restricting its motion in the horizontal direction, towards and away from the cantilever. Then, whenever the cantilever moves towards the spring-loaded magnet, the latter is pushed away due to the repulsive force, increasing the distance between the magnets, thereby reducing the repulsive force required to be overcome for bistable operation. The opposite occurs when the cantilever moves away. Thus, the role of spring-loading is to introduce a type of negative feedback, through the self-adjustment of the distance between the magnets, favoring bistable operation over a larger range of excitations, and this is accomplished without an added energy cost. A 90% gain in power output levels over the fixed magnet system was observed.

CHAPTER I

INTRODUCTION: MOTIVATION AND OBJECTIVES

The development of microelectromechanical systems (MEMS) has ushered in a wide range of applications for miniature sensors and actuators. Further, with the advent of wireless technology, it has been possible to develop wireless sensors for remote applications, such as underground sensors for agricultural purposes [1-4], for example, soil moisture and salinity content [5-6], and structural health monitoring sensors, e.g. bridge monitoring [7-9]. A major concern for such remotely-located devices is extending the life of finite-energy batteries, thereby delaying the need for their replacement.

A potential means of extending battery life is the use of miniature renewable self-contained power supply units, which can convert ambient energy from existing sources in their environment into electrical form, and supplement batteries. Ambient energy may be present in various forms, such as light, thermal, volume flow of liquids or gases, gravitational energy, human motion, and different microbes [10]. Different sources have different energy content. For example, [11] indicates the theoretical limit of electrical power which can be generated from human walking motion using piezoelectric transducers without affecting the gait to be 1.27 W. Smil in [12] lists the average wind power density, measured as the flux of the wind's kinetic energy moving through the area swept by the blades, to be 400 W/m^2, while the average solar radiation flux reaching the Earth's surface to be about 170 W/m^2. As has been calculated later in the section on Future Directions, for a 1 GJ lightning strike 1 km above the ground, the acoustic vibration energy density reaching the ground surface is about 0.8 J/m^2, and that penetrating the ground is about 3.2 mJ/m^2. In order to provide a broader perspective, the following two tables are presented. Table I-1 lists the energy density by volume available from various fuels [13]. Differing from the traditional definition of power density (rate of energy release per unit volume of the energy converter), [12] defines power density as the power released per square meter of horizontal area of land or water surface utilized. Using this definition, Table I-2 lists the power density available from some of the different power sources in use now.

Table I-1: Energy density by volume of various fuels [13].

Fuel	**Energy density by volume (MJ/m^3)**
Wood chips (30% moisture content (MC))	3,100
Log wood (20% MC)	5,200-7,400
Wood (solid, oven dry)	7,600-11,400
Wood pellets	11,000
House coal	23,000-26,000
Anthracite	36,300
Heating oil	36,000
Natural gas	35.2
Liquefied petroleum gas	23,600

Table I-2: Power density of various power sources [12].

Power source	**Power density (W/m^2)**
Natural gas	200-2000
Coal	100-1000
Solar	4-9
Wind	0.5-1.5
Biomass	0.5-0.6

For certain applications, ambient vibrations prove to be a viable option for energy harvesting. For example, wireless underground sensors can make use of ambient vibrations through factors such as thunder or agricultural work on the ground surface, bridge monitoring sensors can make use of bridge vibrations due to the traffic passing over it, and sensors mounted on or inside machines can make use of the mechanical vibrations during operation of the machine.

Such kinetic energy harvesting requires a transduction mechanism to generate electrical energy from motion [11]. The three most commonly used transduction mechanisms for vibration energy harvesting are electromechanical, electrostatic and piezoelectric. A transducer can utilize relative velocity, relative displacement or the mechanical strain within the system for electricity generation. With relative velocity, electromagnetic generators are generally utilized [14-17], while relative displacement is utilized within electrostatic transducers [18-21]. The strain effect uses deformation within the mechanical system, and generally employs active materials such as piezoelectric [22-27].

Electromagnetic harvesting is based on the principle of electromagnetic induction, where an electric current is generated in a conductor, generally in the form of a coil, placed in a magnetic field, when there is a relative motion between a magnet and a conductor. The magnitude of electricity generated depends on the strength of the magnetic field, the velocity of the relative motion, and the number of turns of the coil. Both micro- and macroscale implementations have been reported in literature. Electrostatic harvesting utilizes the energy stored in a capacitor; the work done against the electrostatic force of attraction between the capacitor plates provides the energy to be harvested.

The maximum power density achieved from any of the three methods is theoretically comparable [11], but there are other factors that determine their usability in a practical application. The electromagnetic systems have the limitation that wafer and sub-millimeter scale implementations are difficult. On the other hand, while electrostatic generators are MEMS-realizable, they require a polarizing charge/voltage and suffer from parasitic capacitances [28]. Therefore, we focus on piezoelectric harvesters, which lend themselves to simple implementations, microengineering, and a variety of material choices.

Piezoelectric-based harvester structures may be either linear or nonlinear. In order to maximize the energy transduced from broadband ambient vibrations, this work focuses on nonlinear harvesters. The first part of the work, presented in [29, 30], makes the following contributions:

- Presents for a first time, an accurate mathematical model for a nonlinear bistable transducer by augmenting the Butterworth van Dyke piezoelectric model to capture external magnetic force;
- Combines nonlinear bistable transduction with synchronized energy extraction circuits using electronic breaker switches for efficient harvesting over broadband sources. To the best of our knowledge, this is a first effort reporting the combining of nonlinear transduction with synchronized extraction; and
- Presents the physical implementation of a bistable harvester, and provides experimental validation against simulated results, verifying the enhanced effectiveness of the nonlinear architecture and extraction schemes over the ones reported in literature.

The improved efficiency of the above bistable harvester depends on the harvester operating in the bistable mode. When excitations are large enough to overcome the magnetic repulsive force, the cantilever snaps between its two equilibrium states with increased amplitude and velocity, resulting in higher power outputs. However, low-amplitude excitations are unable to overcome the repulsive force, causing the cantilever to vibrate around one of its equilibrium states with smaller amplitudes in presence of the opposing repulsion. The second part of this work, presented in [31], demonstrates a way to circumvent this issue, and makes the following contributions:

- Presents a completely mechanical way of increasing the bistable range of operation of the harvester, thus increasing efficiency, with close to zero energy cost;
- Extends the nonlinear Butterworth van Dyke model of the piezoelectric transducer with fixed magnet, presented in our previous work [29, 30], to model the modification, namely spring-loading the previously fixed magnet;
- Combines the new architecture with synchronized energy extraction circuits using electronic breaker switches for efficient harvesting over broadband sources;
- Presents physical implementation of a spring-loaded bistable harvester; and
- Provides experimental results, verifying increased amplitude range of bistable operation for a spring-loaded architecture over the fixed-magnet one.

CHAPTER II

BACKGROUND: PIEZOELECTRIC ENERGY HARVESTING

Piezoelectric Materials

A piezoelectric material transduces energy between the electrical and mechanical domains. Application of an electric field across the material creates a mechanical strain and deforms the material. Conversely, the application of a mechanical stress creates an electrical polarization within the material, and this polarization is directly proportional to the applied stress. These materials are available in various forms, which include [11] single crystals (e.g. quartz), piezoceramic (e.g. lead zirconate titanate or PZT), thin film (e.g. sputtered zinc oxide), and screen-printable thick-films based upon piezoceramic powders and polymeric materials (e.g. polyvinylidenefluoride or PVDF).

The piezoelectric strain constant, d_p, is defined as the ratio of the strain developed in the material to the applied electric field, or conversely, as the ratio of the short circuit charge density created to the stress applied [32]. The materials which depend on the application of longitudinal stress perpendicular to the electrodes utilize the d_{33} coefficient, while those that make use of the transverse stress parallel to the electrodes make use of the d_{31} coefficient. The transverse mode of operation is the more favorable mode in energy harvesting, since it provides for mechanical amplification of applied stresses.

Modeling

Since the piezoelectric effect involves transduction of energy between the electrical and mechanical domains, the constitutive equations of a piezoelectric material can be written as (II-1) and (II-2) below, relating two electrical parameters, the electric displacement D (C/m^2) and the electric field strength E (V/m), to two mechanical parameters, the stress σ (N/m^2) and the strain δ (dimensionless) through the electric permittivity of the piezoelectric material at null stress ε_σ (F/m), the elastic compliance at null electric field strength s_E (m^2/N), and the piezoelectric strain constant d_{eff} (C/m^2 or m/V) [33]:

$$D = \varepsilon_\sigma . E + d_{eff} . \sigma \qquad \text{(II-1)}$$

$$\delta = d_{eff} . E + s_E . \sigma \qquad \text{(II-2)}$$

Multiplying (II-1) with unit area and (II-2) with unit length, we get (II-3) and (II-4) respectively, where Q_d is the charge separation, u is the displacement, and V_p is the voltage developed on the piezoelectric material due to the external force applied, F. C_l is the lumped capacitance and k the lumped stiffness constant of the piezoelectric material:

$$Q_d = C_l . V_p + d_{eff} . F \qquad \text{(II-3)}$$

$$u = d_{eff} . V_p + k^{-1} . F \qquad \text{(II-4)}$$

Equivalently,

$$F = k.u - k.d_{eff}.V_p = k \int (velocity) - k.d_{eff}.V_p \equiv \frac{1}{C_m} \int (velocity) - \rho.V_p \qquad \text{(II-5)}$$

$$Q_d = C_l.V_p + d_{eff}.F = C_l.V_p + d_{eff}.\left(k.u - k.d_{eff}.V_p\right) \qquad \text{(II-6)}$$

$$= \left(C_l - k.d_{eff}^2\right).V_p + k.d_{eff}.u \equiv C_e.V_p + \rho.\int (velocity)$$

These equations can be represented as an electrical circuit with forces represented by voltages and velocities by currents, as in Figure II-1, as has been shown in [33]. The primary side models the mechanical behavior and the secondary side the electrical one. The primary side acts as a mechanical spring, with compliance $C_m = 1/k$ equaling the inverse of spring constant of the beam, $\rho = k.d_{eff}$ becomes the transduction ratio of the transformer from mechanical to electrical, and $C_e = C_l - k.d_{eff}^2$, that appears on the electrical side, is the blocked electrical capacitance of the material.

This model, however, does not consider inertia and the inherent losses. The Butterworth van Dyke (BVD) piezoelectric model [32-35], shown in Figure II-2, provides a more complete dynamic model, with three added components: the inertial behavior captured by an inductor M_m, the mechanical damping of the beam by resistor R_m, and dielectric losses by resistor R_e. Note the BVD model views the mechanical (primary) side as a second-order mass-spring-damper system, whose electrical analog represents it as inductor-capacitor-resistor system, where inductance M_m equals the mass, capacitance C_m is the mechanical compliance (the inverse of spring constant), and resistor R_m equals the mechanical damping. On the other hand, the electrical (secondary) side is a capacitive load C_e (where charge is developed) with resistive load R_e (where dielectric losses occur).

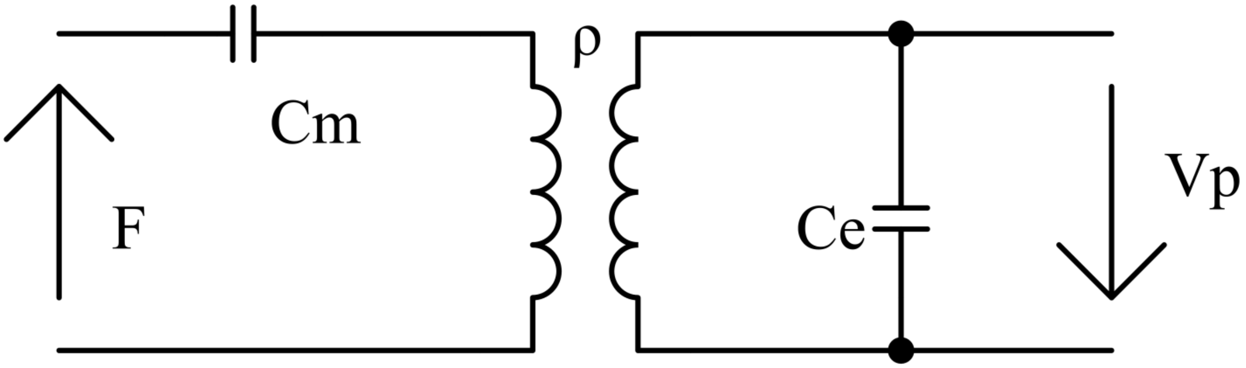

Figure II-1: Equivalent circuit of piezoelectric material assuming no losses.

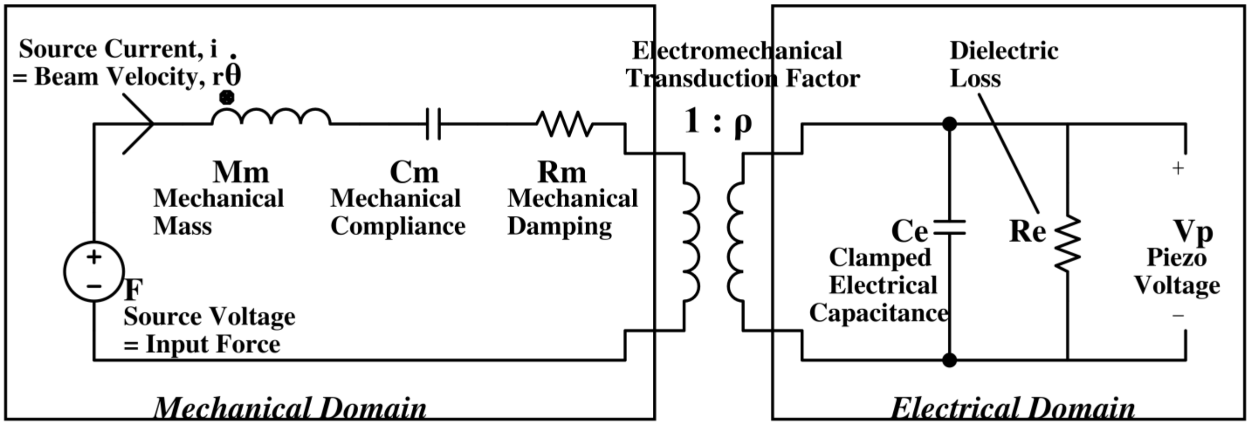

Figure II-2: Lumped electrical model, or Butterworth van Dyke model, of piezoelectric transducer.

Linear Piezoelectric Harvesters

Various methods have been employed to harvest energy from ambient vibrations using piezoelectric materials. Most of these focus on operating at the resonant frequency of the system where the harvester efficiency is the highest [11]. These include the earliest methods of impact coupled devices [22, 23] which have a mass striking against a piezoelectric plate or disc in order to polarize the material, thereby transducing the electrical energy. Umeda *et al.* [22] were able to generate maximum power outputs of 19 µW per impact into a 10 kΩ resistive load for elastic collisions.

Attempts have been made to use human motion to strain piezoelectric materials to extract electrical energy. For example, for a piezoelectric dimorph, consisting of two curved pre-stressed piezoelectric transducers bonded to a metal midplate, mounted in the heel of the shoe, at a 0.9 Hz footfall frequency, an average power of 8.4 mW was produced into a 500 kΩ load [24]. The curved structure makes the transducers compressively stressed, allowing them to deform to a larger extent on application of pressure. Thus, the dimorph deforms when the heel of the shoe hits the ground, and gets back to its original shape as the heel is lifted, both events causing a voltage to be generated.

A common design for piezoelectric generators is the cantilever structure, and a number of variations of this design have been explored. For example, Roundy *et al.* [25] developed a prototype with a piezoelectric shim on each side of a steel beam, and an inertial mass at the tip in order to increase the vibration amplitude and duration. When an external vibration is applied to the structure, the beam vibrates, straining the piezoelectric layers. This structure makes use of the d_{31} bending mode piezoelectric strain coefficient for energy generation. They were able to generate maximum power outputs of 350 μW into a 250 kΩ load with 2.5 m/s^2 input acceleration at 120 Hz resonant frequency.

Other non-conventional piezoelectric-based harvester structures include a cantilever excited using radioactive materials [26], and the use of magnetostrictive materials [27] to strain piezoelectric materials. In the former, a radioactive source, placed underneath the cantilever, radiates β-particles which impinge on the copper sheet attached to the underside of the cantilever, thus charging it electrostatically. As the charge on the copper sheet builds, the electrostatic field increases and the beam is attracted towards the source, till they come in contact and the field is dissipated. The beam is then released to vibrate at its natural frequency and the kinetic energy is used to extract electrical energy from the piezoelectric plate. A peak power of 16 μW was obtained, but the output being extremely periodic, the average power output was less than 1 nW. The other method makes use of magnetostrictive materials, which deform when placed in a magnetic field. The structure consists of a piezoelectric slab sandwiched between two slabs of magnetostrictive material, and a horse-shoe shaped permanent magnet, which is subject to the external vibration. As the magnet moves, the changes in magnetic field cause the magnetostrictive slabs to deform, which in turn creates a stress on the piezoelectric material, and thus generates a voltage which can be extracted.

Broadband Piezoelectric Harvesting

Most ambient vibrations, e.g., thunder or bridge vibrations, are broadband, while linear transducers are efficient only at a single frequency of their natural resonance. One possible way to implement a transducer that remains efficient over broadband would be to use an array of piezoelectric cantilevers with varying resonant frequencies. For example, Xue *et al.* [36] were able to show that the operating frequency band of a cantilever-based harvester can be widened by connecting a number of cantilevers with different piezoelectric material thicknesses, and hence different resonant frequencies, in series to form a branch, and the position of this band can be adjusted to match the input frequency band by adjusting a number of such branches of cantilevers in parallel. However, this results in a large overall size of the system, while at any given frequency, only one cantilever operates efficiently. This compromises the power density of the system. A more viable solution is the use of nonlinear structures, which are able to produce larger oscillations over a wider frequency range as compared to linear systems [37-39], and hence operate efficiently over a wide band of excitation. An implementation of a nonlinear system is a bistable system, which has two equilibrium positions. In our work, we have made use of one such nonlinear structure, in the form of a bistable cantilever, so as to produce high power outputs over a wide range of frequencies, as will be discussed in the following chapter.

CHAPTER III

BISTABLE VIBRATION ENERGY HARVESTER WITH SYNCHRONIZED POWER EXTRACTION

Broadband Bistable Harvester Implementation

Figure III-1 shows a simple way of realizing a bistable system with a cantilever and two magnets with the same polarities facing each other, one at the cantilever tip, and the other fixed [40]. Due to the repulsive force between the magnets, the cantilever bends away from the horizontal axis, in essence shifting its equilibrium position from horizontal. The shift can occur either above or below the horizontal axis, presenting two equilibrium states, symmetric to the horizontal axis. Configured this way, the cantilever vibrates in one of the two equilibrium positions for small excitations that are unable to overcome the magnetic repulsive force. However, for larger excitation, the cantilever is able to snap back and forth between the two equilibrium positions. This effectively increases the vibration amplitude and velocity for the same input excitation, hence the voltage and power outputs, as compared to linear operation. This increase in vibration amplitude and velocity has also been shown and analyzed in [40-45].

For the bistable snap-through mechanism, the increase in harvested power is observed for frequencies lower than the linear resonance of the system [41]. For the system to respond effectively to an input, the rise-time (time to travel from zero-displacement to maximum displacement) must be much smaller than the rise-time of the input oscillation (which is a quarter of the time period). This condition is satisfied roughly when the input frequency is smaller than natural frequency (so rise-time of input is larger than rise-time of displacement). Hence, the maximum input frequency for increased output would be limited to be about the linear resonant frequency of the cantilever system. Also, the spread of the output frequency spectrum reduces as compared to the input, making the power extraction easier.

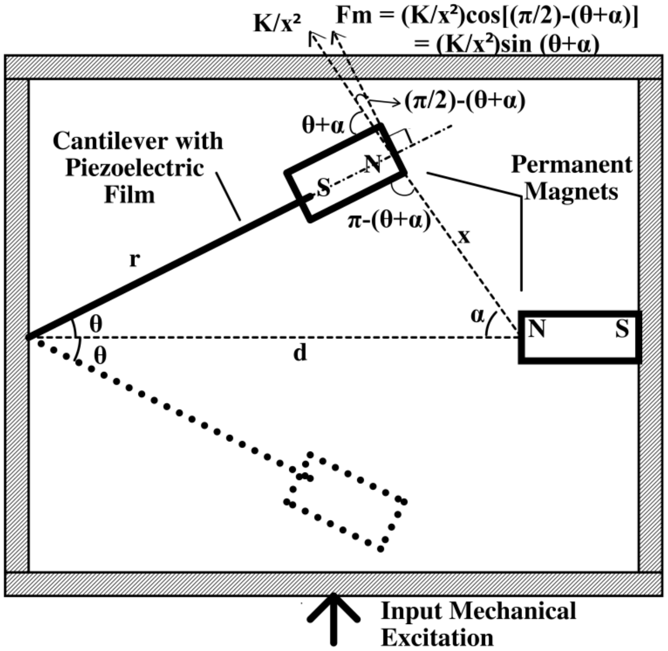

Figure III-1: Bistable system formed by cantilever and two magnets. The cantilever is at one of the equilibrium positions, while the other position is symmetrically opposite, shown in dotted lines.

Proposed Bistable System Modeling

Authors in [40] modeled the bistable system by adding a nonlinear spring to the linear spring-mass model of the resonant system. Although it serves the purpose, this model is a heuristic one. We propose an accurate model by adding a correct form of nonlinearity to the linear Butterworth van Dyke (BVD) model, introduced in Figure II-2, noting that the BVD model represents forces as voltages and velocities as currents. The nonlinearity in the bistable system, presented in the previous section, is introduced by the externally-applied nonlinear magnetic force alone, and in its presence, the source voltage, which represents the total input force *F*, is a sum of the externally applied vibration force, F_v, and the nonlinear magnetic force,

F_m. The source current i, on the other hand, represents the velocity of the beam and equals $rd\theta/dt$, which is the product of length r of the cantilever with its angular velocity. Accordingly, the model is described by (III-1) for the primary (mechanical) and (III-2) for the secondary (electrical) side:

$$F = F_m + F_v = M_m \frac{di}{dt} + \frac{1}{C_m}\int idt + iR_m + \frac{V_p}{\rho}, \tag{III-1}$$

$$C_e \frac{dV_p}{dt} + \frac{V_p}{R_e} = \frac{i}{\rho}, \tag{III-2}$$

where V_p/ρ is the secondary voltage reflected on the primary through the transduction factor (or turns ratio) ρ; i/ρ is the primary current reflected on the secondary side. Note that the magnetic force along the line connecting the two magnets is K/x^2, where x is the distance between the two magnetic poles as shown in Figure III-1, and $K = (\mu q_1 q_2/4\pi)$ is a constant of proportionality depending on the strengths of magnetic poles q_1 and q_2, and medium permeability μ. So its component normal to the beam is $F_m = (K/x^2).\cos[(\pi/2)-(\theta+\alpha)] = (K/x^2).\sin(\theta+\alpha)$; see Figure III-1. From the property of angles, $\sin(\theta+\alpha) = \sin[\pi-(\theta+\alpha)]$, and from the property of triangles, $\sin[\pi-(\theta+\alpha)] = (d/x).\sin\theta$, where d is the distance between the fixed supports, and so $F_m = (K/x^2)(d/x)\sin\theta = (K/x^3)d\sin\theta$. Also, from another property of triangles, $x=(r^2+d^2-2.r.d.\cos\theta)^{1/2}$, and therefore, $F_m=(K.d.\sin\theta)/x^3 =(K.d.\sin\theta)/(r^2+d^2-2.r.d.\cos\theta)^{3/2}$. Using this, and replacing i with $rd\theta/dt$ (recall in BVD, current corresponds to beam velocity) in equations (III-1) and (III-2), we finally get (III-3) and (III-4) that models the bistable transducer:

$$\begin{aligned} F = F_m + F_v &= \frac{Kd\sin\theta}{(r^2+d^2-2rd\cos\theta)^{3/2}} + F_v \\ &= M_m r\frac{d^2\theta}{dt^2} + r\frac{\theta}{C_m} + R_m r\frac{d\theta}{dt} + \frac{V_p}{\rho}, \end{aligned} \tag{III-3}$$

$$C_e \frac{dV_p}{dt} + \frac{V_p}{R_e} = \frac{1}{\rho} r \frac{d\theta}{dt}. \tag{III-4}$$

In the absence of vibrational force ($F_v = 0$), the beam is stationary at one of its equilibrium angles θ_0, under the action of the magnetic force F_m balanced by the restoring spring force $r\theta/C_m$ (recall that $r\theta$ is the displacement and $1/C_m$ is the spring constant). In the equilibrium, the velocity and acceleration of the cantilever are zero. Also, even though the cantilever is bent, the voltage developed on the capacitor C_e eventually dissipates through the resistance R_e, and so in the stationary state, the piezoelectric voltage V_p is also zero. Hence, substituting $F_v = 0$, $d\theta/dt = 0$, $d^2\theta/dt^2 = 0$ and $V_p = 0$ in (III-3) leads us to the equilibrium equation (III-5), solving which, we can calculate the initial deflection θ_0:

$$\frac{K.d.\sin\theta_0}{(r^2 + d^2 - 2.r.d.\cos\theta_0)^{3/2}} = r\frac{\theta_0}{C_m}. \tag{III-5}$$

To validate our model, the above mathematical model was simulated in Matlab Simulink (Mathworks Inc.) [46], for a sinusoid input excitation of 1.63 N, 10 Hz (acceleration of 500 m/s^2). The parameter values as listed in Table III-1 are those for a real piezoelectric cantilever harvester Volture V21B by Midé [47], of dimensions 69.1 mm x 16.8 mm x 0.64 mm (piezoelectric dimensions 35.56 mm x 14.48 mm x 0.2 mm), that we also used for experimental validation. These values were calculated from the physical and material properties of the cantilever, using expressions provided in [34], such as $C_m = \frac{1}{E}\frac{4L^3}{wt^3}$, $R_m = 2\xi\sqrt{\frac{M_m}{C_m}}$, $R_e = \frac{1}{\tan\delta(2\pi f_n C_e)}$, and $d_{eff} = \frac{E_p d_{31} w_p (2c - t_p) L_p}{EI}\left[L - \frac{L_p}{2}\right]$, where L, w, t, E and L_p, w_p, t_p, E_p are the length, width, thickness and elastic modulus of the beam and the piezoelectric material, respectively. ξ is the mechanical damping ratio, $\tan\delta$ is the loss tangent, I is the moment of inertia, and f_n is the natural frequency of the beam. d_{31} is the piezoelectric coefficient, and c is the location of the neutral axis from the bottom of the beam. M_m and C_e are the mass and electrical capacitance of the cantilever. All of the above values were provided by the manufacturer. $K = \frac{\mu q_1 q_2}{4\pi} = \frac{\mu}{4\pi}(B_1 A_1)(B_2 A_2)$ was calculated using the flux linkage between the magnets, which can be assumed to be the same as the flux at their surfaces, if they are placed very close. B_1, B_2 are the magnetic field strength and A_1, A_2 are the surface area of the two magnets, respectively. The physical and material properties are listed in Table III-2.

Table III-1: Butterworth van Dyke model parameter values for Volture V21B piezoelectric cantilever harvester.

C_m (m/N)	R_m (N·s/m)	M_m (kg)	C_e (nF)	R_e (MΩ)	r (mm)	d (mm)	K (N·m^2)	d_{eff} (m/V)	$\rho = C_m/d_{eff}$ (V/N)
$5.865*10^{-4}$	$4.8*10^{-3}$	$3.26*10^{-3}$	4	106.1	35.56	36.5	$9.33*10^{-7}$	$3.165*10^{-7}$	1852.536

Table III-2: Physical and material properties of the Volture V21B piezoelectric cantilever harvester.

L (mm)	w (mm)	t (mm)	E ($*10^{10}$ Pa)	ξ ($*10^{-3}$)	tan δ	d_{31} ($*10^{-12}$ m/V)	f_n (Hz)
35.56	16.764	0.635	7.144	1.018	0.0013	190	275
L_p (mm)	**w_p (mm)**	**t_p (mm)**	**E_p ($*10^{10}$ Pa)**	**$A_1 = A_2$ ($*10^{-5}$ m^2)**	**$B_1 = B_2$ (T)**	**I ($*10^{-12}$ kg.m^2)**	**c (mm)**
35.56	14.478	0.4064	6.7	3.167	0.1212	0.589	0.318

The Simulink mathematical model was built using the various Simulink blocks, such as mathematical operators and sources, so as to simulate and solve the set of equations (III-3) - (III-5). The model to solve (III-5), shown in Figure III-2, was first used to calculate θ_0, which was then used to solve (III-3) and (III-4) to find the displacement θ and the piezoelectric output voltage V_p, based on the input excitation applied, as shown in Figure III-3.

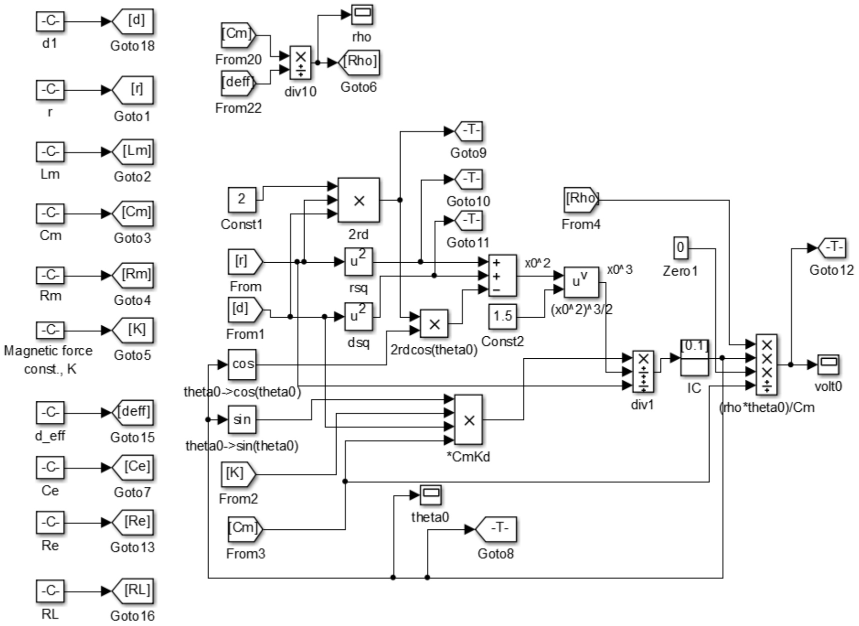

Figure III-2: Simulink model to solve for initial displacement.

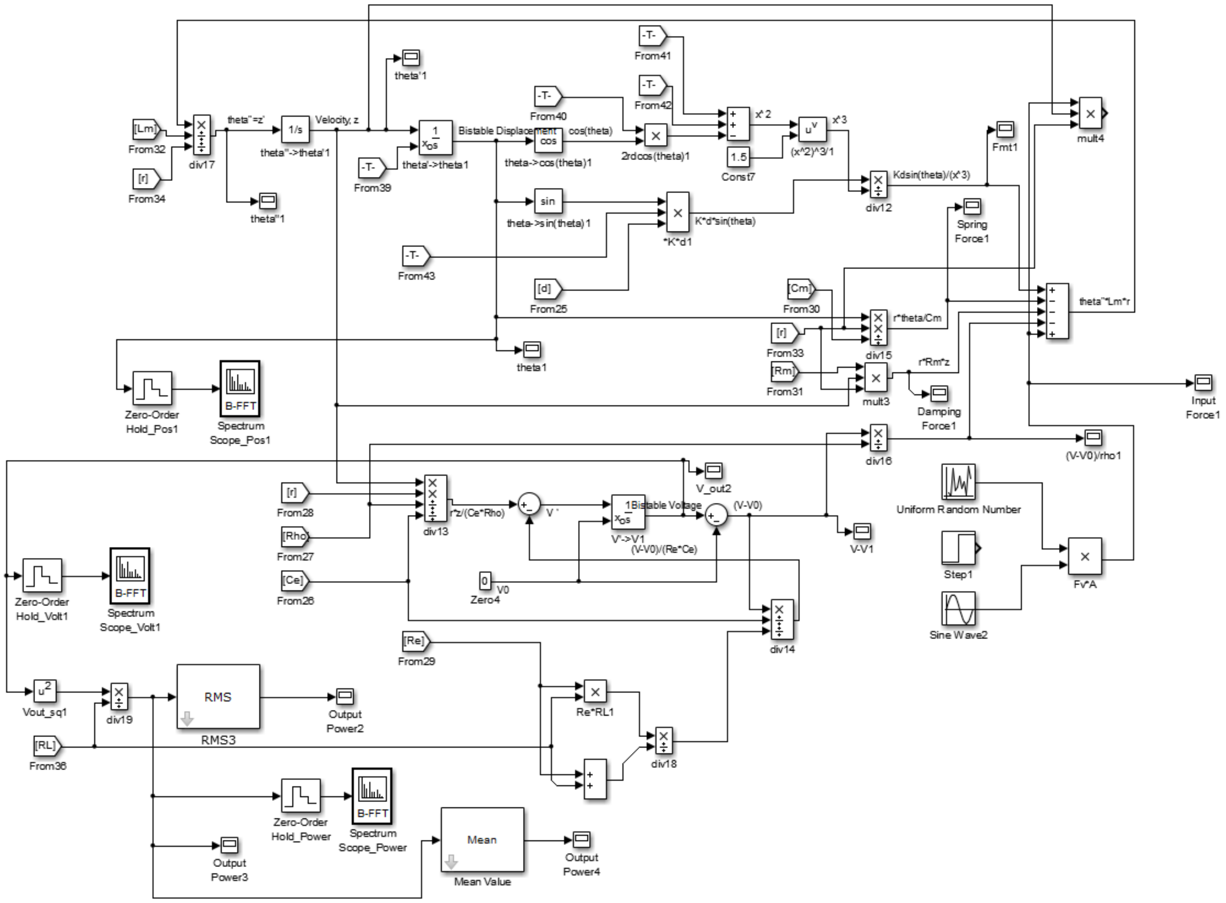

Figure III-3: Simulink mathematical model of the bistable piezoelectric cantilever.

Figure III-4 compares the displacement and open-circuit voltage plots for linear monostable operation with no magnets used, and nonlinear bistable operation with the magnets. Since the input is a sinusoidal excitation, the output follows a similar trend. We measure the amplitudes of vibration and of the open circuit voltage to compare performances. For the input excitation, the magnetic force and the distance between the magnets used, the plots show about 30% increases in both the measured amplitudes for bistable operation. For validation of our mathematical model, we employed PSpice to simulate the circuit-model of Figure II-2 under the same operating conditions; the plots are shown in Figure III-5, where the nonlinear magnetic force is modeled as a nonlinear capacitor. (Note that the magnetic force, represented as voltage, is a nonlinear function g of displacement: $F_m = g(r\theta)$, and since displacement is integral of velocity, which represents current, we have: *voltage = g(integral of current)*, which is indeed the generic relation for a nonlinear capacitor.) The plots of Figure III-5 are almost identical to those from simulation of our proposed mathematical model on Simulink (see Figure III-4), thereby validating our proposed model.

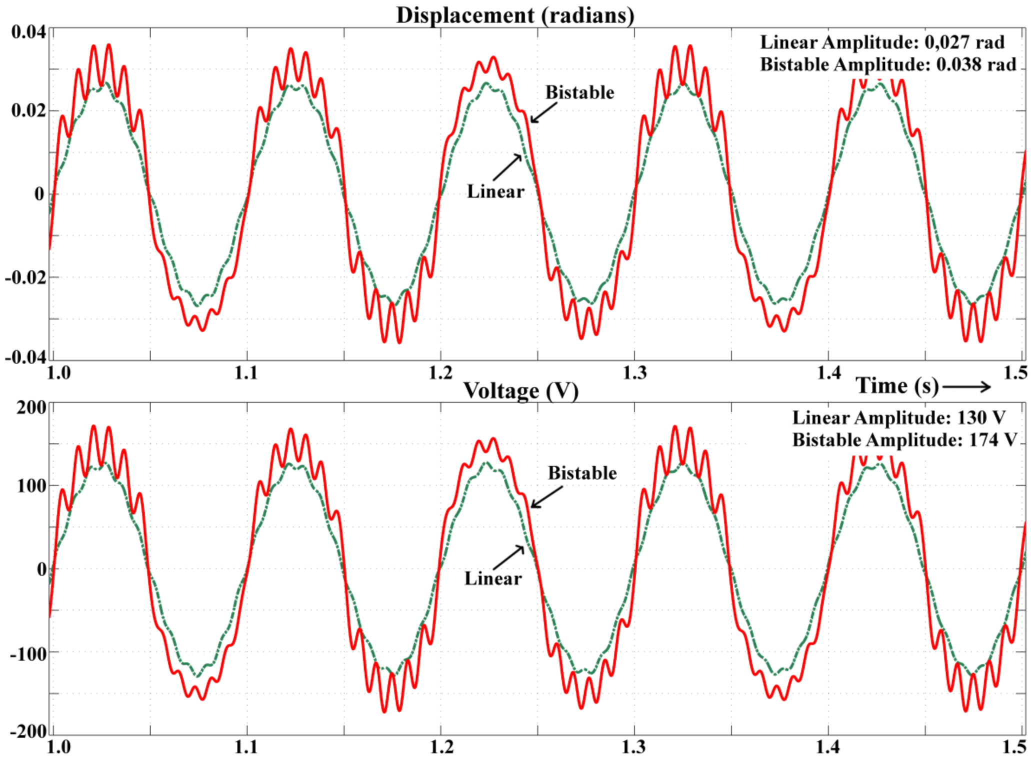

Figure III-4: Displacement (radians) and open circuit voltage (Volts) plots for linear and nonlinear bistable operation, as obtained from simulations on Matlab Simulink.

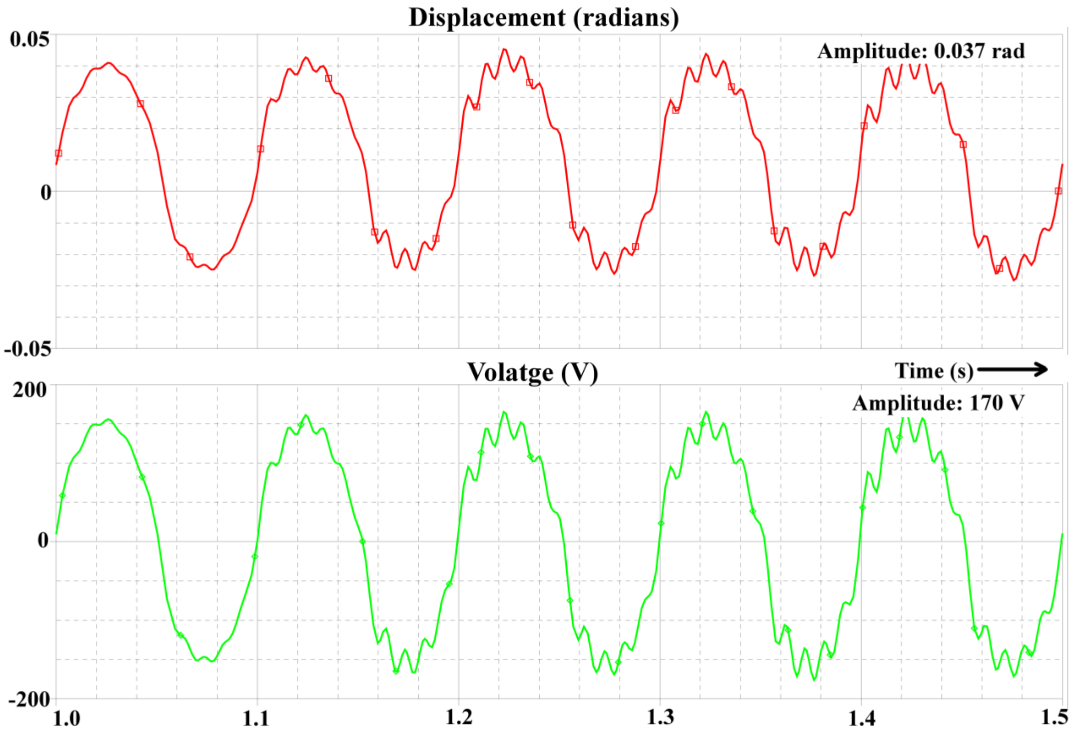

Figure III-5: Displacement (radians) and open circuit voltage (Volts) for nonlinear bistable operation, as obtained from simulating the proposed BVD-based model in PSpice.

Power Extraction Circuits

The introduction of bistable nonlinearity helps achieve a significant gain (30% for the input force used) in the vibration amplitude and open circuit piezoelectric voltage, and hence the energy available for extraction, as seen through simulations. However, since the electric energy source is nonlinear, standard ways to extract energy from linear sources turn out to be inefficient. Various extraction schemes for the piezoelectric generator have been proposed [48-52]. This section presents methods we have utilized to optimize power extraction from our nonlinear bistable transducer [29-31], and compares them to a standard extraction circuit comprising an AC to DC converter. Since the extracted energy is required to charge a battery, all circuits analyzed have a battery as the load. Also, since the ambient vibrations are time-varying, the piezoelectric transducer output is also non-dc, necessitating the use of a rectification step to be able to charge a dc battery.

Standard extraction circuit

The standard extraction circuit uses only a rectifier [50, 51]. In the standard circuit of Figure III-6, the piezoelectric voltage V_p is fed through the bridge rectifier formed by diodes D_1-D_4 to the battery with voltage V_b. As the input force F increases, charge builds up on C_e till the point where V_p becomes greater than V_b by two diode drops V_D. At this point, the battery begins to get charged. The energy added into the battery at piezo-voltage V_p is given by (III-6). Then the average power P into the battery is given by (III-7) for a sinusoidal input with frequency ω. Differentiating P with respect to V_b and setting it to zero, we can find the optimal value of the battery voltage, $V_{b\text{-}opt}$, for maximum harvested power, is half the maximum open circuit piezoelectric voltage, V_{pm}, reduced by the voltage drop across the diodes, as in (III-8). Setting V_b to this value in (III-7) gives us the maximum power which can be harvested, as in (III-9).

$$E_{inst} = \begin{cases} \frac{1}{2}C_e(|V_p| - V_b - 2V_D)V_b, & |V_p| > V_b + 2V_D \\ 0, & otherwise \end{cases} \tag{III-6}$$

$$P_{avg} = \frac{2C_e\omega V_b}{\pi}(V_{pm} - V_b - 2V_D) \tag{III-7}$$

$$V_{b-opt} = \frac{1}{2}(V_{pm} - 2V_D) \tag{III-8}$$

$$P_{max} = \frac{2C_e\omega V_{b-opt}^2}{\pi} = \frac{C_e\omega\left(V_{pm} - 2V_D\right)^2}{2\pi} \tag{III-9}$$

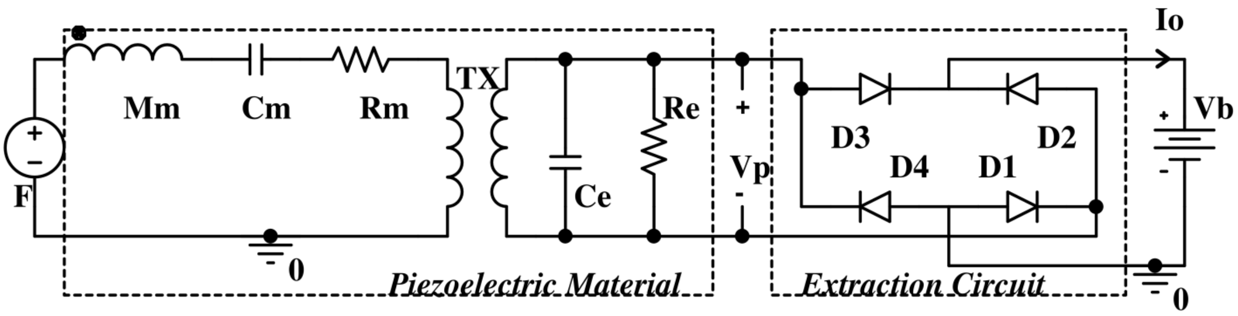

Figure III-6: Standard energy extraction circuit.

It should be noted here that the nonlinear bistable operation increases the vibration amplitude and velocity, thus V_p and V_{pm}, nonlinearly, resulting in more harvested power than from linear transducers reported in literature [50]. The operation of the bistable harvester is shown in the plots of Figure III-7 for a sinusoidal input of 0.326 N, 10 Hz (acceleration of 100 m/s^2).

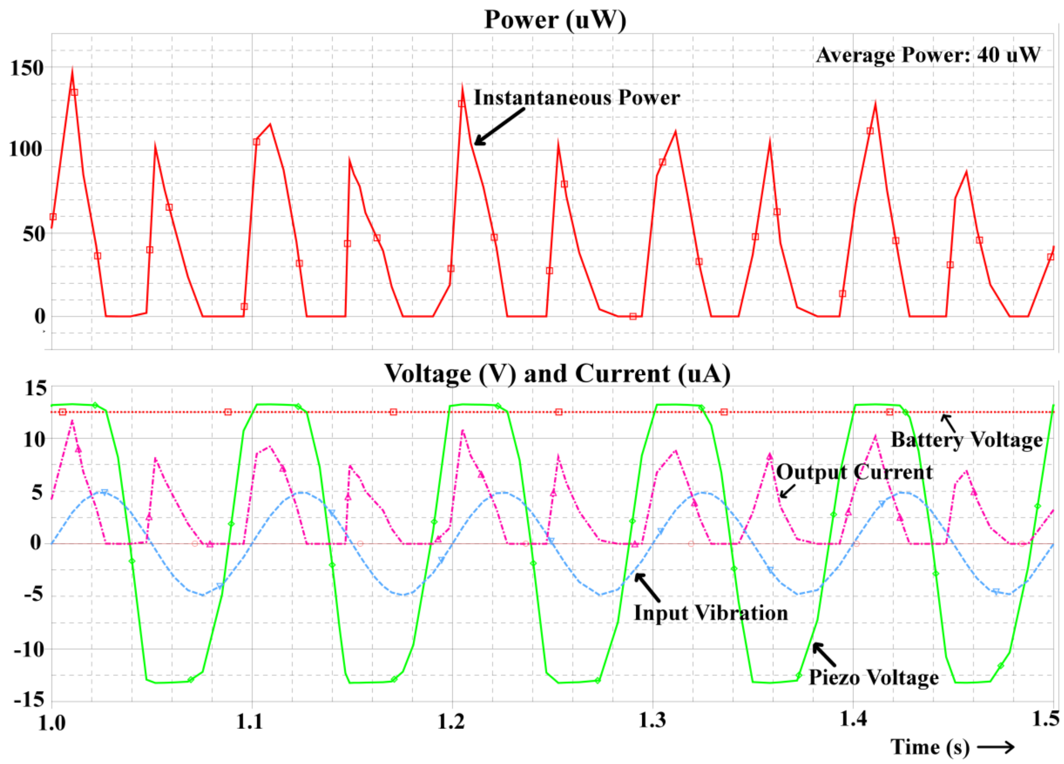

Figure III-7: Simulation plot for standard circuit, showing the displacement (qualitatively) and the corresponding voltages (V), current (µA) and power flowing into the battery (µW). For a sinusoidal input of 0.326N, 10Hz to the nonlinear bistable harvester, average harvested power is about 40µW.

Synchronous Charge Extraction (SCE)

The synchronous charge extraction (SCE) circuit [50, 51], employed in our work [29-31], allows charge to build up on the piezoelectric capacitance C_e until it reaches a maximum, corresponding to the maximum displacement of the cantilever. At this point, all the charge is extracted from the capacitor and transferred to the battery, thereby dropping the piezoelectric voltage to zero. Thus the charge is extracted synchronously with it reaching its maximum, and this synchronized extraction leads to improved efficiency as discussed below.

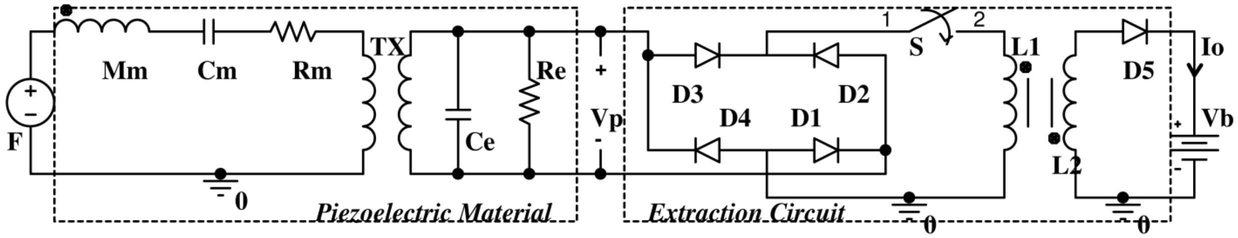

Figure III-8: Synchronous charge extraction (SCE) circuit.

In the SCE circuit of Figure III-8, switch *S* remains open normally while electrostatic energy builds up on C_e as the piezo-cantilever moves from zero displacement to one of the extrema. *S* is closed at the displacement extrema, transferring the energy stored in C_e to the primary winding L_1 of the coupled inductor as magnetic energy. When the transfer is complete, the capacitor voltage drops to zero, typically in a quarter of the time period of the oscillator L_1-C_e. Here, we have chosen L_1 such that the L_1-C_e oscillator time period is three orders of magnitude lower than the intended range of values for the input excitation period *T*. As a result, the charge transfer is orders of magnitude faster compared to *T*. When all the charge is transferred, *S* is turned off again, and the magnetic energy trapped in the coupled inductor flows in only one direction, namely to the battery through diode D_5 as electrical energy.

For sinusoidal F_v, the piezoelectric open circuit voltage has amplitude V_{pm}, and in going from one extremum to the next, the piezoelectric capacitor C_e undergoes a voltage change of $2V_{pm}$. However, with the SCE circuit, the piezoelectric voltage V_p goes to zero at the displacement extrema by transferring all charge on C_e to the inductor, and rises from zero as the cantilever moves from one extremum to the next in the opposite direction. Thus, between the two adjacent extrema, C_e undergoes the voltage change of $2V_{pm}$, and since V_p starts at zero, its amplitude increases to $2V_{pm}$. Also, all the charge thus generated, is extracted to charge the battery, leading to the increased extracted power. The electrostatic energy stored on C_e at the extrema is given by (III-10), and the average power P flowing into the battery by (III-11), where T is the input excitation time period. The average power is independent of the battery voltage and always maximized with respect to it; hence SCE is a “self-optimized” extractor. In practice, non-idealities, such as quality factor of the inductor and diode voltage drops, affect the extracted power [51].

$$E = \frac{1}{2} C_e \left(2V_{pm}\right)^2 = 2C_e V_{pm}^2 \tag{III-10}$$

$$P = \frac{2}{T} E = \frac{2}{\pi} \omega C_e V_{pm}^2 \tag{III-11}$$

In order to realize a self-propelled, low-power switch S that triggers at displacement extrema, the electronic breaker circuit [52-54] was used. As SCE architecture requires rectification prior to extrema detection, only maxima need to be detected. The corresponding switching circuit of Figure III-9 includes an envelope detector with a storage capacitor C_s, a comparator with the PNP transistor Q_1, and a switch with NPN transistor Q_2. The signal at the envelope detector charges C_s to the envelope voltage. Q_1 remains blocked while the envelope voltage at its emitter is less than the signal voltage at its base, thus blocking Q_2. When the signal voltage starts falling as the cantilever changes direction of motion after the extremum, the envelope voltage remains constant at the highest value reached, since the charge on C_s is unable to discharge. When the signal voltage falls below the envelope voltage, Q_1 turns on, allowing C_s to discharge and turn on Q_2 in the process; thus turning on the switch. Figure III-10 shows a breaker in an SCE circuit. When the current through Q_2 falls to zero, the tendency of the L_1-C_e oscillator is to reverse current direction. However, the diode D_8 prevents this reversal, turning the switch off, thus providing automatic control of switch on-time; this is necessary in this architecture in order to maximize the energy harvested.

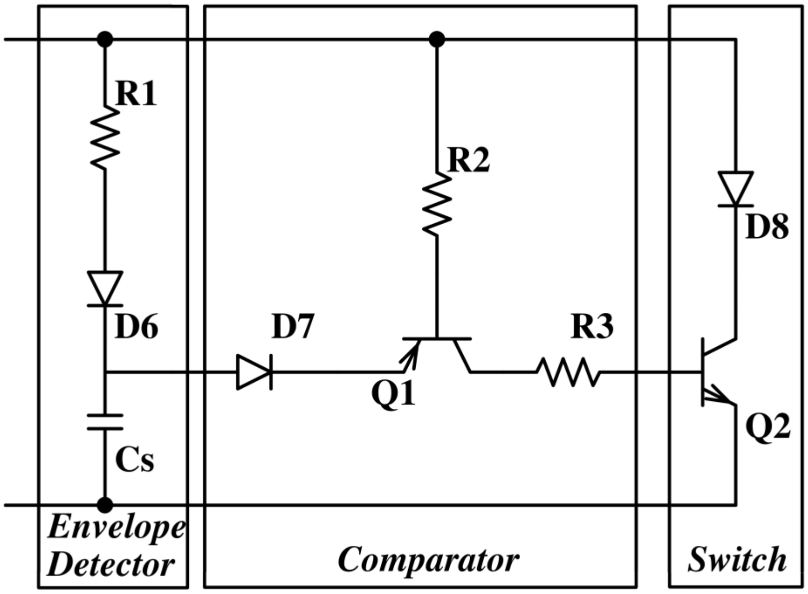

Figure III-9: Electronic breaker circuit for switching on at maxima displacement.

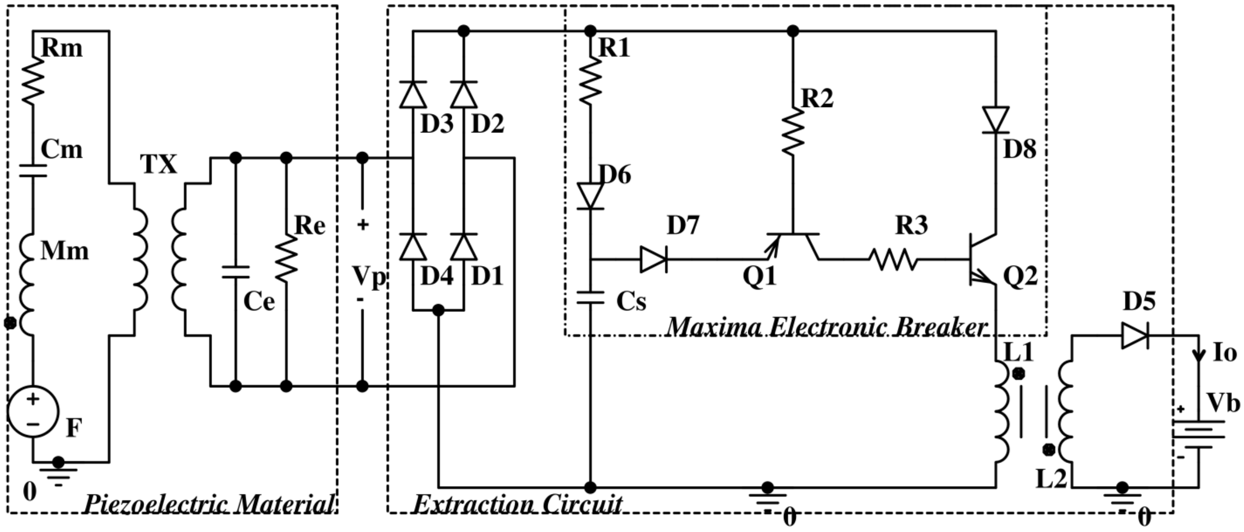

Figure III-10: SCE circuit with the electronic breaker.

The ratio of the voltage on C_s, V_{Cs}, to the piezoelectric voltage is given by $\frac{V_{Cs}}{V_p} = \frac{1}{\sqrt{1+\omega^2 {C_s}^2 (R_1+R_D)^2}} \tan^{-1}[-\omega C_s(R_1+R_D)]$, as presented in [53]. According to the equation, there is a phase delay between the two voltages, dependent on R_1, C_s and R_D, where R_D is the forward resistance of the diode. The corresponding time delay can be calculated to be $(\tan^{-1}[-\omega C_s(R_1 + R_D)])/\omega$. For V_{Cs} to follow V_p closely, the magnitude of the ratio should ideally be 1, and the phase should be 0, requiring low R_1, C_s and R_D values.

The operation of the SCE circuit is shown in the plots of Figure III-11 for a sinusoidal input of 0.326 N, 10 Hz (acceleration of 100 m/s^2). The current and power flowing into the battery appear as pulses at the instant the switch is turned on. The slight delay of about 8 ms observed in the plot in turning the switch on at an extremum is due to the voltage drop across the diodes, as well as the threshold voltage of the transistors.

It should also be noted that the delay, τ, in turning on the switch would limit the operating frequency of the circuit. For this extraction circuit to operate efficiently, the switching needs to occur before the piezoelectric voltage drops to zero, meaning that quarter of the time-period of oscillation should be greater than the delay, i.e., $T > 4\tau$, or $f < 1/4\tau$. Figure III-12 shows the voltages and currents in the coupled inductor and the power into the battery at the instant the switch is turned on.

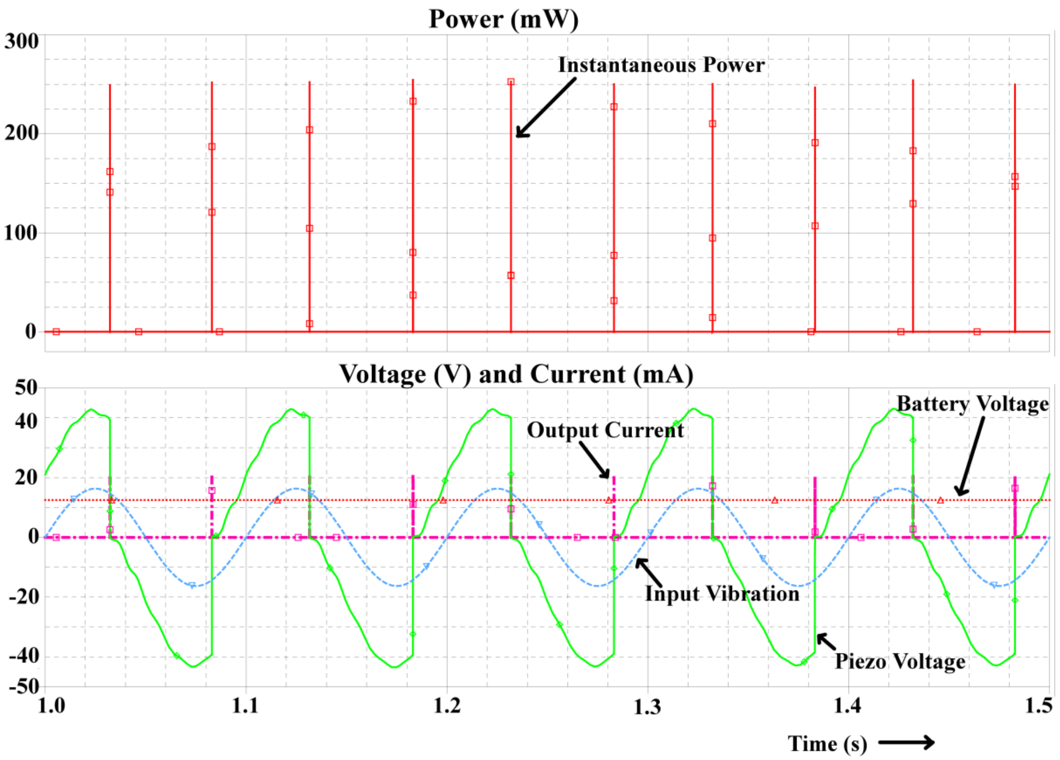

Figure III-11: Simulation plot for SCE circuit, showing the displacement (qualitatively) and the corresponding voltages (V), current (mA) and power flowing into the battery (mW). For a sinusoidal input of 0.326N, 10Hz to the nonlinear bistable harvester, average harvested power is about 80µW.

Parallel Synchronized Switch Harvesting on Inductor (SSHI)

The parallel synchronized switch harvesting on inductor (SSHI) circuit [50, 51], employed in our work [29-31], also involves switching at displacement extrema for synchronized extraction. Unlike SCE, however, the switch is turned on at the extrema to invert charge polarity on the piezoelectric capacitor, while the charge developed on C_e flows to the battery during the rest of the period. Thus parallel SSHI extracts charge for a longer period than SCE, but clamped at battery voltage level, whereas in SCE charge transfer happens at a higher piezoelectric voltage (twice the maximum open circuit piezoelectric voltage) but that occurs almost instantaneously.

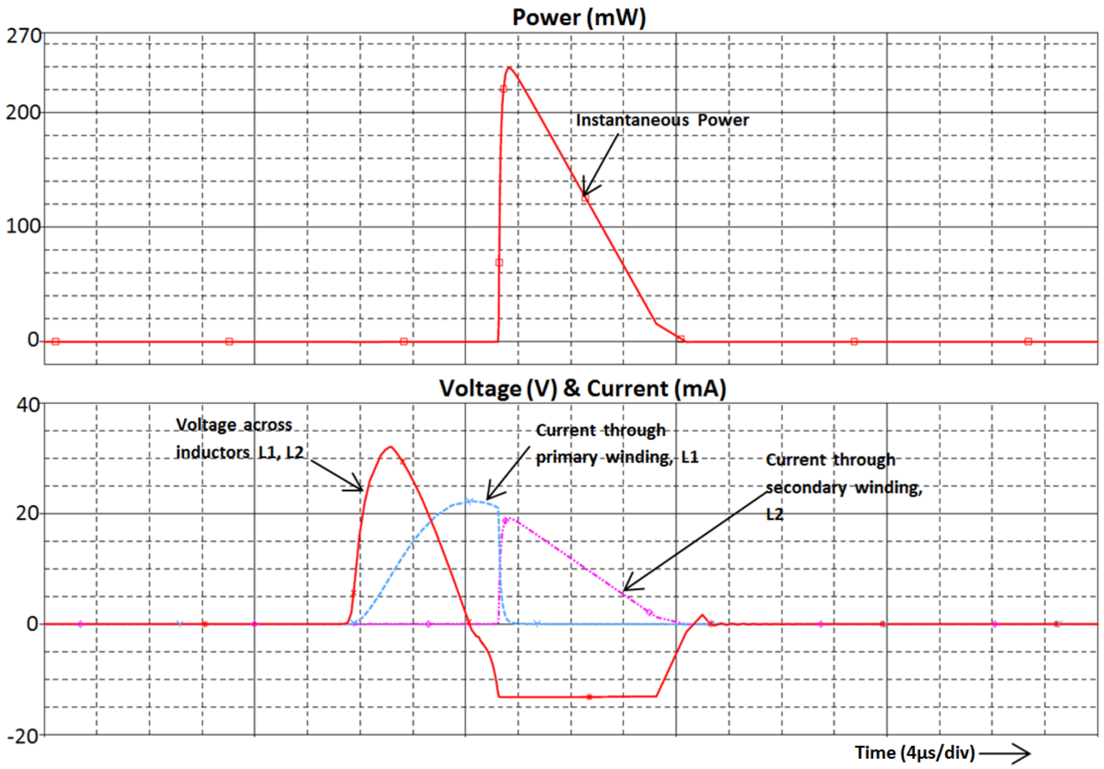

Figure III-12: A zoomed-in view of the voltages, currents and power at the instant the switch is turned on.

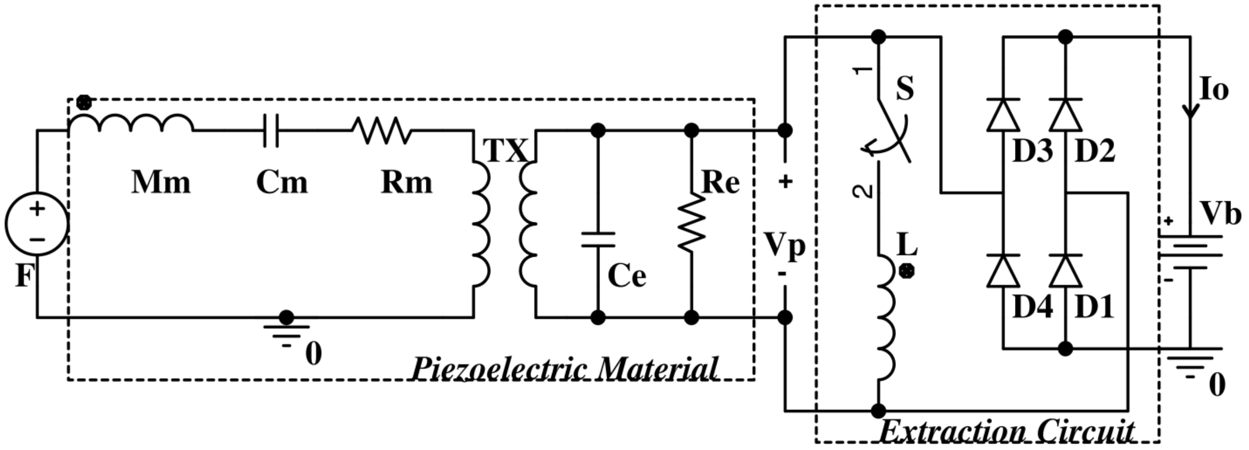

Figure III-13: Parallel synchronized switch harvesting on inductor (SSHI) circuit.

In the parallel SSHI circuit of Figure III-13, switch *S* remains open normally, and the battery charges while V_p is greater than V_b. At a displacement extremum, *S* is closed to form an L-C_e oscillator, and is kept on for half the L-C_e time-period to let the voltage on C_e, clamped at V_b due to the battery, invert in polarity through the inductor *L*. The time period of the L-C_e

oscillator is kept much smaller than the input excitation period T in order to allow fast reversal of polarity on C_e; we chose the L-C_e period to be three orders of magnitude smaller than T. During this inversion, the bridge diodes remain reverse biased, and the battery is not charged. Once S is opened after the voltage reversal on C_e is complete, C_e is charged again in the opposite direction, and on reaching a magnitude of V_b, the bridge diodes start conducting, resuming charging the battery. This allows the charging of the battery for the entire duration until a next extremum is reached, nearly half of the time-period, minus the time taken for charge inversion.

Ideally, the polarity inversion on C_e would be perfect, and the voltage would flip between $+V_b$ and $-V_b$, charging the battery for the full duration the switch is off. However, due to the finite quality factor Q of the inductor, the inversion is not perfect, and is determined by (III-12), where V_{inv} and V_{init} are the voltages after and before inversion. Further, some charge Q_c is needed to raise V_p to V_b before charging of the battery starts, given by (III-13). This inversion of polarity on C_e results in V_p rising up to the battery voltage much faster than in the linear case, and thus charging the battery for a longer duration, ultimately resulting in increased power extraction.

For a sinusoidal input, energy E flowing into the battery over half the time period $T/2$ is given by (III-14) and the average power P by (III-15). The optimum battery voltage $V_{b\text{-}opt}$ in (III-16) for maximum power transfer is calculated by differentiating P with respect to V_b in (III-15), and the corresponding maximum power P_{max} is given by (III-17). As before, V_{pm} refers to the open circuit piezoelectric voltage amplitude.

$$V_{inv} = -V_{init}e^{-\pi/2Q} = -V_b e^{-\pi/2Q} \tag{III-12}$$

$$Q_c = C_e V_b\left(1 - e^{-\pi/2Q}\right) \tag{III-13}$$

$$E = \left(2C_e V_{pm} - C_e V_b\left(1 - e^{-\pi/2Q}\right)\right)V_b \tag{III-14}$$

$$P = \frac{2}{T}E = \frac{\omega}{\pi}\left(2C_eV_{pm} - C_eV_b\left(1 - e^{-\pi/2Q}\right)\right)V_b \tag{III-15}$$

$$V_{b-opt} = \frac{V_{pm}}{\left(1 - e^{-\pi/2Q}\right)} \tag{III-16}$$

$$P_{max} = \frac{\omega C_e}{\pi}\frac{V_{pm}^2}{\left(1 - e^{-\pi/2Q}\right)} \tag{III-17}$$

In the case of SSHI, two electronic breakers are used for switching, as the switch is placed before the rectifier, hence requiring the detection of both maxima and minima. The electronic breaker for minima switching control is obtained from modifying the one for the maxima breaker by inverting the polarities of diodes and transistors in Figure III-9. In the parallel SSHI circuit with electronic breakers of Figure III-14, after displacement maxima (resp., minima), V_p falls below the envelope voltage on C_{s1} (resp., C_{s2}), hence Q_1 (resp., Q_4) starts conducting, turning on Q_2 (resp., Q_3). After polarity inversion on C_e, the reversal of current direction in the oscillator L-C_e is prevented by diode D_8 (resp., D_9), turning the switch off automatically.

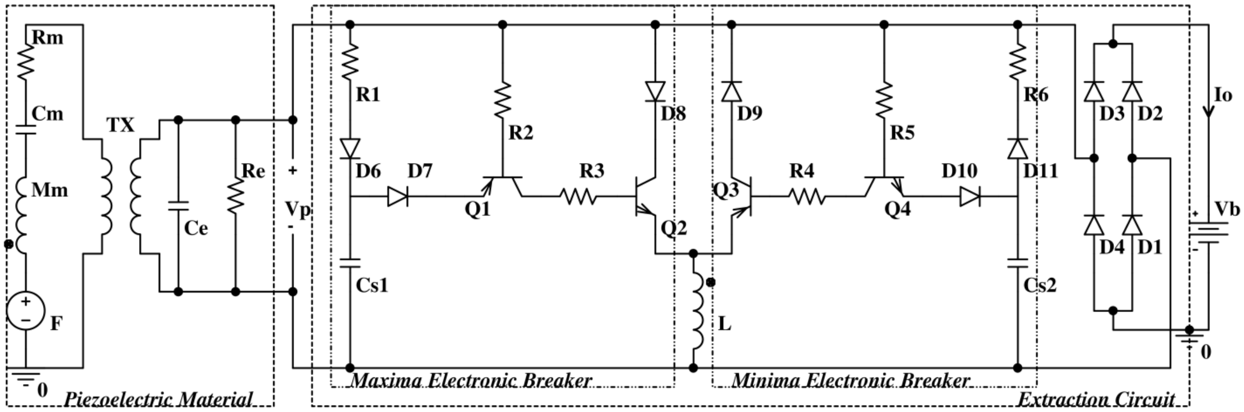

Figure III-14: Parallel SSHI circuit with maxima and minima electronic breakers.

The parallel SSHI operation is shown in the plots of Figure III-15 for a sinusoidal input of 0.326 N, 10 Hz (acceleration of 100 m/s^2). At the displacement extrema, the reversal of piezoelectric voltage on C_e is not perfect; some charge is required to raise V_p up to the battery voltage V_b, during which no power flows into the battery. Once at V_b, the rectifier diodes begin to conduct, charging the battery. The delay of about 3 ms in turning the switch on after reaching the extrema is due to the diode voltage drops, and the threshold voltages of the transistors, as explained above for the SCE case.

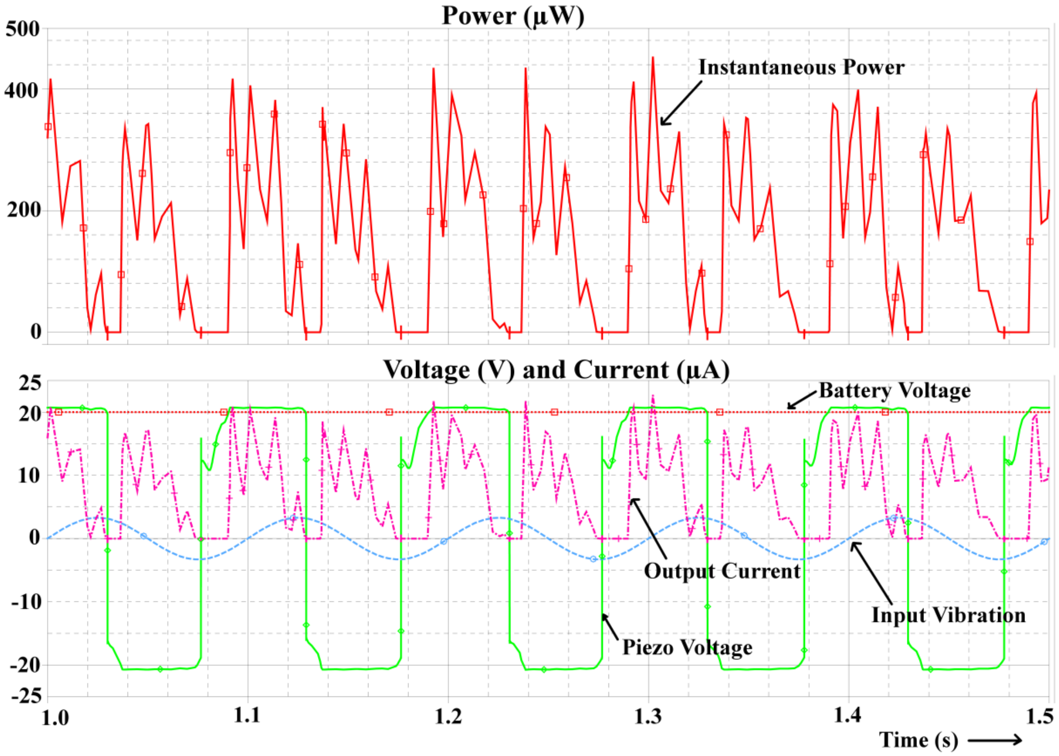

Figure III-15: Simulation plot for SSHI circuit, showing the displacement (qualitatively) and the corresponding voltages (V), current (µA) and power flowing into the battery (µW). For a sinusoidal input of 0.326N, 10Hz to the nonlinear bistable harvester, average harvested power is about 125µW.

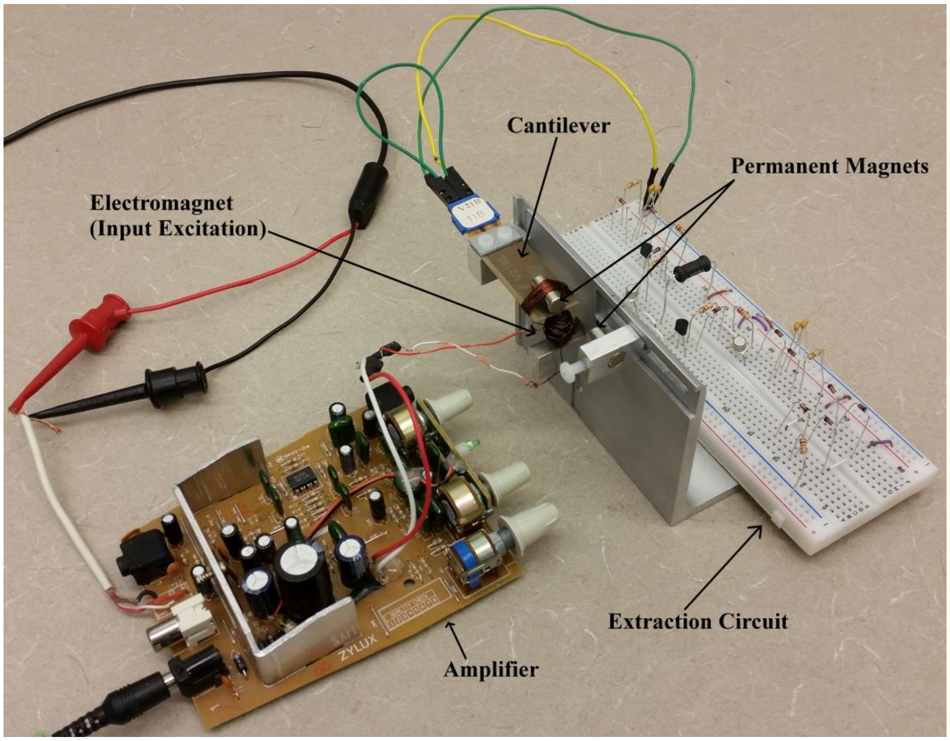

Figure III-16: Experimental setup for the bistable harvester.

Simulated and Experimental Results

Experimental setup

The experimental setup that we prototyped is shown in Figure III-16, and the measurement setup for the experiments is shown in Figure III-17. It uses the piezoelectric cantilever Volture V21B by Midé [47], mentioned above. This cantilever was chosen since it is readily commercially available, and its parameter values are also available from the manufacturer. The cantilever was vibrated using an electromagnet, consisting of an insulated wire wound around a ferrite core, and fed by an amplified signal from a function generator. The placement of the electromagnet is adjustable to allow the adjustment of the input excitation. As explained earlier, the bistability in the circuit was introduced using two permanent magnets

(PMs) with the same poles facing each other. The PM on the cantilever tip not only helps establish bistability, it further helps realize the mechanical vibration as induced by the varying magnetic force from the electromagnet driven by a signal generator. Increasing the distance between the PMs sufficiently, so as to remove the repulsive force, results in a linear cantilever. The output from the cantilever was transferred to the battery through the extraction circuit built on a breadboard, as shown in Figure III-16.

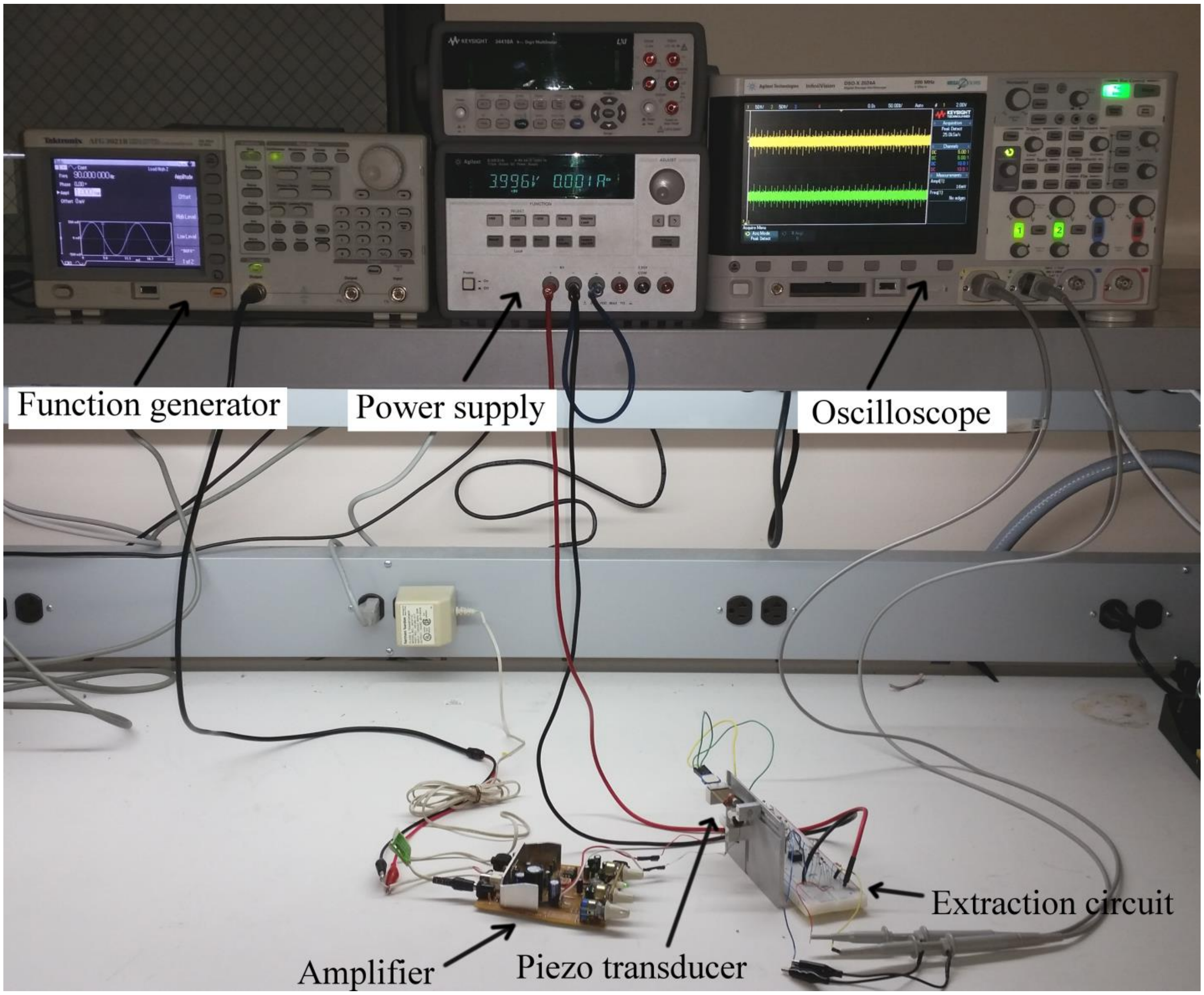

Figure III-17: Measurement setup for the experiments.

The components used in the extraction circuits are detailed in Table III-3. Since we want the inversion of charge on the piezoelectric capacitor in the SSHI circuit, or the extraction of charge in the SCE circuit, to occur fast in comparison to the input vibration, we choose the inductance value to be low, of the order of 10 mH. The transformer used in the SCE circuit was DA103C with an inductance of 6 mH, and the inductor used in the SSHI was 10 mH, resulting in an L-C_e oscillation frequency of the order of 10 kHz. Further, from the expression for V_{Cs}/V_p for an electronic breaker given earlier, in order for the envelope voltage to follow the piezoelectric voltage closely, V_{Cs}/V_p should ideally have a magnitude 1 and phase 0, requiring C_s, C_{s1}, C_{s2}, R_1 and R_6 to be low. Also, the chosen values of R_2, R_3, R_4 and R_5 ensure that the emitter-base voltages of the transistors do not interfere with the voltages of the envelope detector and the storage capacitors; therefore their values are chosen to be much smaller than R_1 and R_6. The diodes used were 1N4148, the PNP transistors were 2N2907A and the NPN were 2N3904.

Table III-3: Component values for SCE and SSHI circuits.

SCE Circuit			**SSHI Circuit**		
C_s	**R_1**	**R_2, R_3**	**C_{s1}, C_{s2}**	**R_1, R_6**	**R_2, R_3, R_4, R_5**
470 pF	47 kΩ	1 kΩ	200 pF	100 kΩ	1 kΩ

Table III-4: Harvested power from different extraction circuits for sinusoidal input of 0.326 N, 10 Hz.

Type	**Output (μW)**	**Gain over Standard Linear**	**Power Density (mW/cm^3)**
Standard, Linear	26.5	1	0.036
Standard, Bistable	41.5	1.57	0.056
SCE, Linear	40	1.51	0.054
SCE, Bistable	78.5	2.96	0.105
SSHI, Linear	60	2.26	0.081
SSHI, Bistable	125	4.72	0.168

Results

The simulation results of the powers harvested, gain over optimized linear extractor, and power density from each circuit discussed above have been compared in Table III-4. The SSHI during nonlinear bistable operation has the best gain of 4.72. A sinusoid vibration of 0.326 N, 10

Hz, corresponding to an acceleration of 100 m/s^2, was used for these simulations. We note that (a) nonlinearity increases the power output, and (b) SCE and SSHI circuits increase power extraction over the standard rectifier circuit.

Table III-5 compares some outputs reported in literature to the simulated output from our parallel SSHI-based nonlinear bistable harvester for the same vibrational input. The two final columns of Table III-5 show the “power gain” over the reported output, and the power density of our harvester; the largest gain is 166 times, while smallest one is 3.17 times.

Table III-6 shows that for an arbitrarily chosen sinusoid input excitation of 0.146 N, 90 Hz, corresponding to an acceleration of 45 m/s^2, the simulated and experimental power outputs from the different extraction circuits are in very good agreement, further validating our model. The output plots obtained experimentally for each extraction circuit, shown in Figure III-18 - Figure III-20 are similar in form to the theoretically obtained plots. Assuming the soil sensor reported in [3] transmits once a day for a minute, it was estimated to consume about 1.7 mW. If the harvester is operated at the above mentioned level of continuous sinusoid input, the parallel SSHI circuit for bistable operation could provide 22.65% of the sensor power requirement.

Table III-5: Performance comparison of parallel SSHI (P-SSHI) bistable harvester with reported outputs.

Reference	**Type**	**Input Excitation**	**Output (mW)**	**Size (mm^3)**	**Power Density of reported (mW/cm^3)**		**Bistable Harvester Output (mW)**	**Power Gain over reported**	**Power Density of Bistable Harvester (mW/cm^3)**
Badel *et al.* [48]	P-SSHI (Single crystal piezo)	3.2km/s^2 900 Hz	1.8	40x7x1.5	4.28		7.5	3.17	10.1
Badel *et al.* [48]	P-SSHI (piezo ceramic)	3.2km/s^2 900 Hz	0.09	40x7x1.5	0.21		7.5	82.3	10.1
Badel *et al.* [48]	SCE (piezo ceramic)	3.2km/s^2 900 Hz	0.04	40x7x1.5	0.095		7.5	166	10.1
Lallart *et al.* [50]	SSHI with Electronic Breaker	1mm displ., 106.1 Hz	0.05	40 mm long	-		14	149	18.8

Table III-6: Simulated vs. experimental power outputs for sinusoidal input of 0.146 N, 90 Hz.

Type	Simulated Output (μW)	Experimental Output (μW)	Gain over Standard, Linear	Power Density (mW/cm^3)
Standard, Linear	172	172.68	-	0.232
Standard, Bistable	270	269.52	1.56	0.363
SCE, Linear	30	22.6	-	0.04
SCE, Bistable	340	320.24	1.85	0.458
SSHI, Linear	250	253.75	1.47	0.336
SSHI, Bistable	370	385.02	2.23	0.498

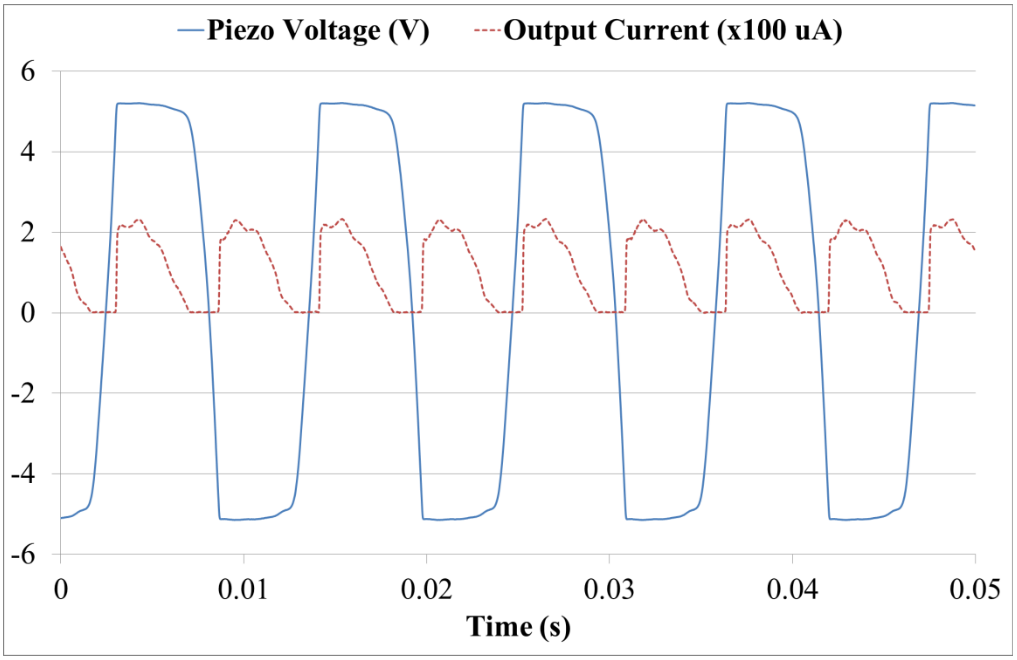

Figure III-18: Experimental plots for the standard circuit during bistable operation.

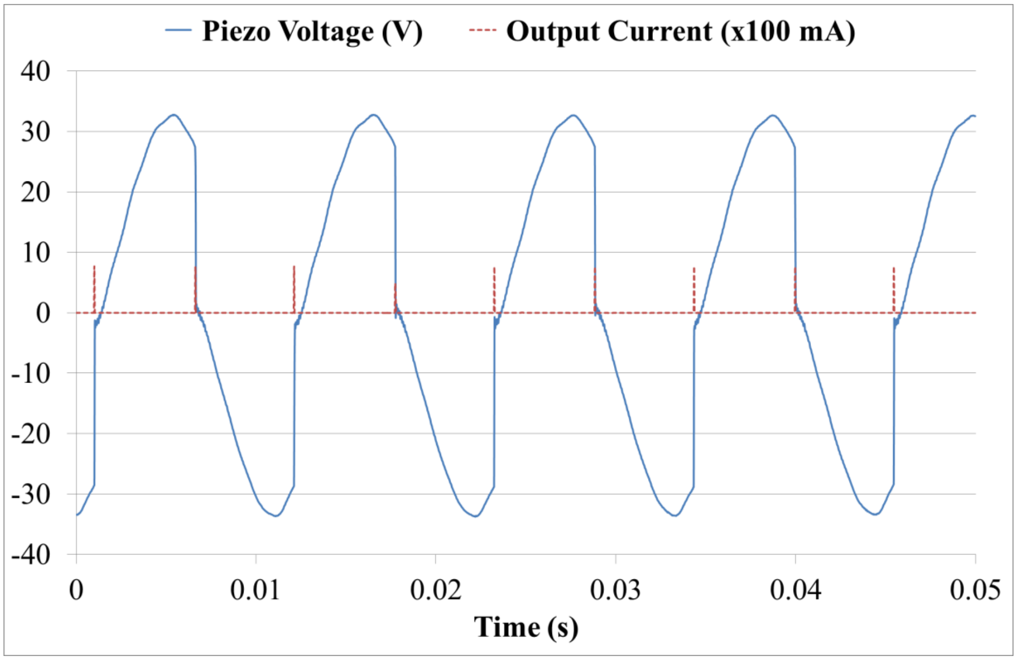

Figure III-19: Experimental plots for SCE circuit during bistable operation.

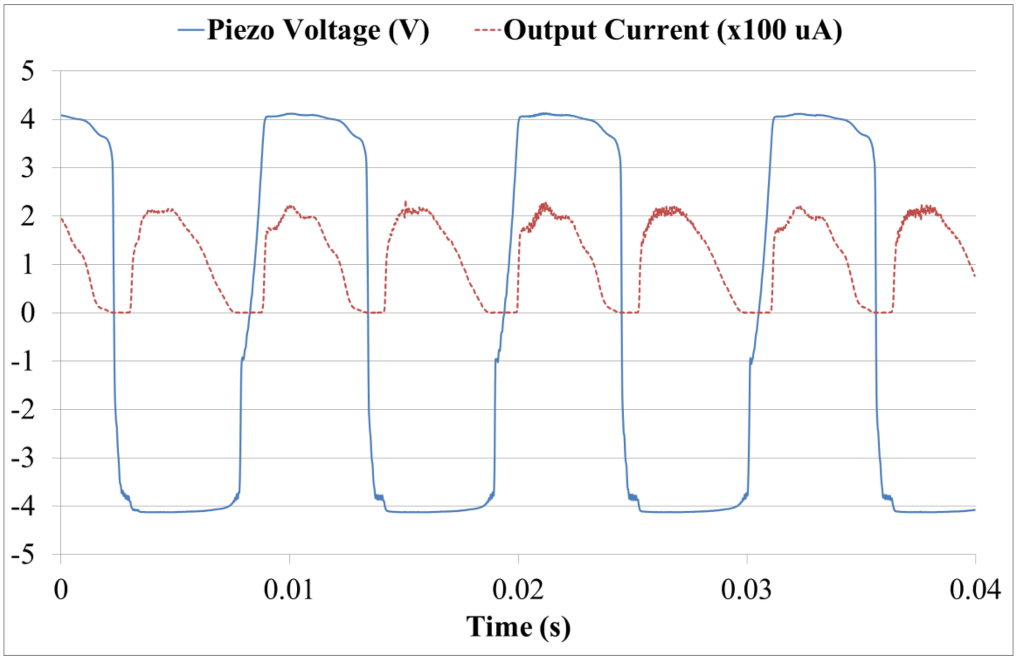

Figure III-20: Experimental plots for SSHI circuit during bistable operation.

Frequency dependence of harvester performance

For measuring harvester performance, we use the ratio of output power to input acceleration, i.e., the “system gain”, and plot its frequency dependence in Figure III-21 for an input of 45 m/s^2. It is seen that nonlinearity leads to increase in harvested power over linear operation in all the three extraction cases over a wide frequency range, up to about 110-120 Hz, which happens to be the resonant frequency of the cantilever with the magnet as the inertial mass, as calculated from (III-18) [34], and consistent with [41]. It follows that the operating frequency range can be adjusted by changing the resonance frequency of the cantilever. We also note that except for SCE at low frequencies, there is a considerable increase in harvested power from the nonlinear extraction circuits for the input excitation used, and while SSHI operation peaks at a particular frequency, SCE provides high outputs over a significantly wider frequency range. Table III-7 lists the peaking frequency and the 3-dB bandwidth for the different circuits.

$$f_n = \frac{1}{2\pi}\sqrt{\frac{1}{C_m M_m}} \tag{III-18}$$

Table III-7: Peaking frequency and 3-dB bandwidth for an input of 0.146 N, 90 Hz.

Type	Peaking Frequency (Hz)	3-dB Bandwidth (Hz)
Standard, Linear	109.5	1.5
Standard, Bistable	109	1.5
SCE, Linear	120	20
SCE, Bistable	118	20
SSHI, Linear	112	1.2
SSHI, Bistable	111.5	1

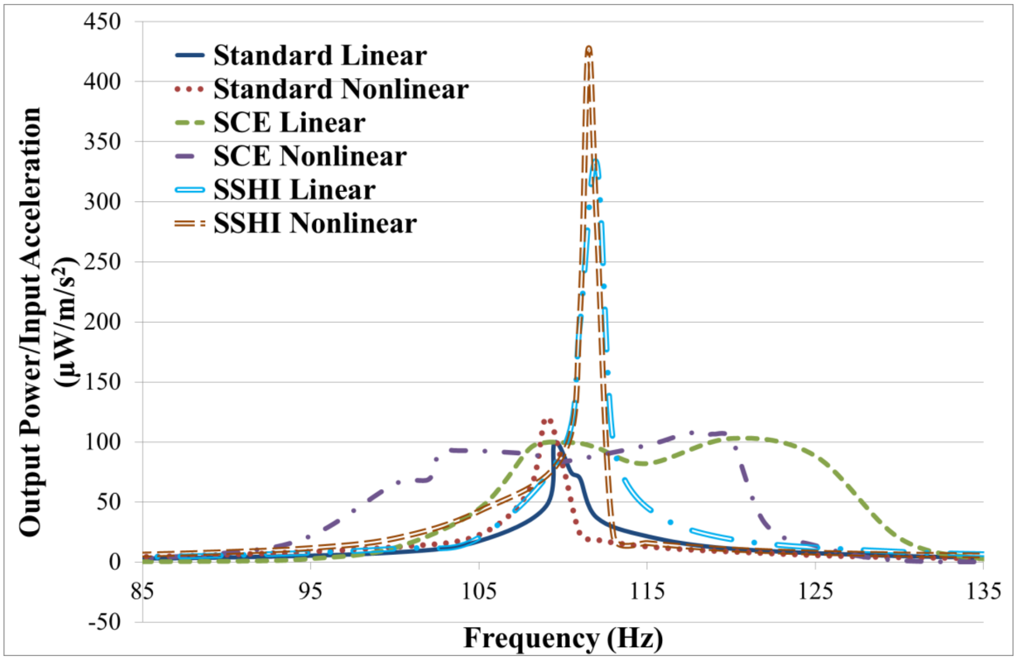

Figure III-21: Frequency variation of ratio of output power to input acceleration for 0.146 N input amplitude.

Harvester Performance for broadband excitations

Table III-8 shows the experimentally achieved power outputs for a broadband excitation. The broadband signal used was a multitone, with frequencies varying from 1 to 95 Hz at 1 Hz intervals, as shown in Figure III-22. This broadband signal was chosen since a number of ambient vibration sources have similar low frequency spectrum. For example, bridge vibrations have their spectral content mostly in the low frequency range of 1 – 40 Hz [8, 9], and thunder vibrations have their dominant frequency in the 100 Hz range [55]. The power output gain over the standard circuit operating in the linear mode is seen to be higher in case of a broadband signal than in case of single frequency; while we achieved gains of less than 5 in Table III-4 and Table III-6 for single frequency excitation, gains as high as 34 in the SCE, bistable operation case and 9 in the SSHI, bistable operation case were observed in Table III-8. We also see nonlinear bistable operation resulting in about 5 to 7 times greater output power than that from linear operation for all three extraction circuits, thus validating that nonlinearity does in fact help improve performance for broadband excitations.

Table III-8: Experimental power output levels for multitoned broadband input.

Type	Power Output (μW)	Gain over Standard, Linear	Power Density (mW/cm^3)
Standard, Linear	52.38	1	0.071
Standard, Bistable	357.12	6.82	0.481
SCE, Linear	264	5.04	0.355
SCE, Bistable	1794	34.25	2.415
SSHI, Linear	129.72	2.48	0.174
SSHI, Bistable	478.98	9.14	0.645

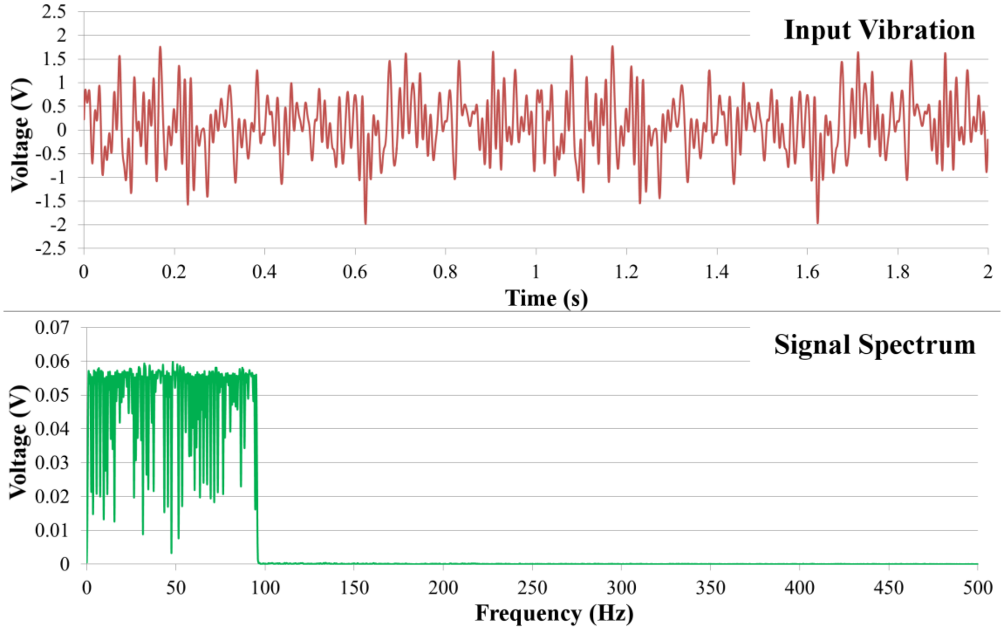

Figure III-22: Broadband multitone signal and spectrum used in the experiment.

CHAPTER IV

BISTABLE HARVESTER WITH SPRING-LOADED MAGNET

Structure

The bistable harvester presented in the previous chapter gives improved performance over a linear harvester whenever it operates in the bistable mode, regardless of the excitation frequency. This requires the external vibration applied to be large enough so as to overcome the repulsive magnetic force. Otherwise, when the input excitation is unable to overcome the magnetic repulsive force, the harvester vibrates in the monostable mode at one of its stable equilibrium positions, in which case the efficiency can be worse than a linear harvester due to the interference from the magnetic force to the excitation force. In order to ensure that the harvester remains in the bistable mode over a wider range of input amplitudes, we envision that the magnetic force be changed adaptively: it be decreased when the input vibration decreases, thus lowering the magnetic force to be overcome, while it be increased with increase in input vibration, thus improving efficiency through increased vibration amplitude and velocity.

Such tuning of the magnetic force can be realized using different methods. One possibility would be to use an electromagnet instead of one of the permanent magnets (PMs), and change the current flowing through the coils in response to the change in input vibration to tune the magnetic force. However, the operation of an electromagnet requires a lot of power, and would compromise the overall efficiency of the system. Another approach would be to reactively adjust the distance between the PMs in response to input excitation, using e.g. linear actuators. This approach would again involve high power costs for actuation, and hence, compromise efficiency.

Here we propose a completely mechanical way of adaptively tuning the distance between the PMs, with close to zero energy cost, by spring-loading the previously fixed PM and restricting its motion in the linear horizontal direction by placing it inside a cylindrical sleeve, as shown in Figure IV-1. As the cantilever moves towards the horizontal position, the PM on spring is pushed inwards due to the compression of the spring caused by the repulsive force, increasing the distance between the magnets, and thereby reducing the magnetic force. As the cantilever moves away, the repulsive force decreases, and the spring relaxes, pushing the PM closer to the cantilever thereby increasing the magnetic force. Thus the spring-loading provides for a type of negative feedback, altering the distance between the PMs in a way that favors an increase in the range of bistable operation.

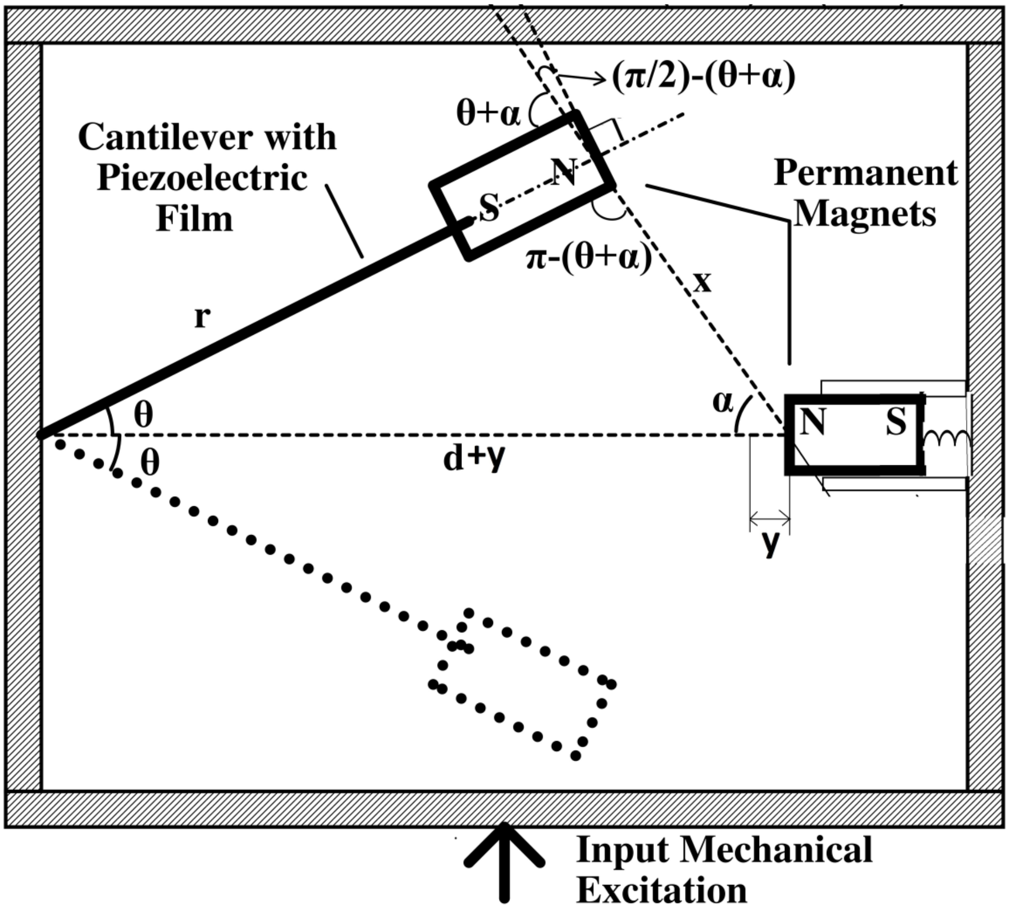

Figure IV-1: Bistable system with spring-loaded permanent magnet.

Modeling of the Bistable Harvester with Spring-loaded Magnet

The model for the spring-loaded magnet system is structurally similar to the BVD model of Figure II-2. However, the expression for the magnetic force F_m, needs to account for the adaptively changing magnetic force due to the varying spring compression. Letting y denote the amount of spring compression, we note the horizontal distance between the PM on spring and the fixed cantilever base is $d+y$, as opposed to d in the fixed magnet harvester case. So replacing d with $d+y$ in (III-3) and (III-4), and also including, for the sake of completeness, the effect of gravity on the PM on the cantilever tip, which provides an extra force $mg\cos\theta$, we get (IV-1) and (IV-2):

$$
\begin{aligned}
F &= F_m + F_v - mg\cos\theta \qquad \text{(IV-1)}\\
&= \frac{K(d+y)\sin\theta}{\left(r^2+(d+y)^2-2r(d+y)\cos\theta\right)^{3/2}} + F_v - mg\cos\theta\\
&= M_m r\frac{d^2\theta}{dt^2} + r\frac{\theta}{C_m} + R_m r\frac{d\theta}{dt} + \frac{V_p}{\rho},
\end{aligned}
$$

$$
C_e\frac{dV_p}{dt} + \frac{V_p}{R_e} = \frac{1}{\rho}r\frac{d\theta}{dt}. \qquad \text{(IV-2)}
$$

Further, writing down the equation of motion for the spring-loaded magnet, we get (IV-3):

$$
\begin{aligned}
\frac{K}{x^2}\cos\alpha - F_f - k_{sp}y &= \frac{K}{x^2}\frac{(x^2+(d+y)^2-r^2)}{2x(d+y)} - \mu_k\left|\frac{Kr\sin\theta}{x^3}+mg\right| - k_{sp}y \qquad \text{(IV-3)}\\
&= m\frac{d^2y}{dt^2}
\end{aligned}
$$

where from the triangle cosine law, $\cos\alpha=(x^2+(d+y)^2-r^2)/2x(d+y)$, and k_{sp} is the spring constant. F_f represents the force of friction acting on the magnet, and is the product of the coefficient of kinetic friction, μ_k, and the net reaction force acting on the magnet due to the cylindrical sleeve, which would be an algebraic sum of the weight of the magnet, mg, and the vertical component of the magnetic force, $(K/x^2).sin(\alpha)=(K/x^2)(r/x)sin\theta=(K/x^3)rsin\theta$. This magnetic force component would act vertically downwards or upwards depending on the inclination of the cantilever being upwards or downwards, and hence add to or subtract from the weight of the magnet. Since the frictional force would always oppose the motion, we use the absolute value of the sum to calculate friction. Equations (IV-1)-(IV-3) provide three equations in four unknowns: θ, x, y, and V_p. A fourth equation is obtained from noting the following relation (IV-4) among x, y, and θ, that is a property of triangles:

$$x^2 = r^2 + (d+y)^2 - 2r(d+y)\cos\theta. \qquad \text{(IV-4)}$$

In the absence of an external vibration force, the cantilever rests at an equilibrium angle θ_0, and the spring-loaded magnet rests with the spring having an equilibrium compression y_0, causing the friction force to fall down to its static value, with coefficient of static friction μ_s. In this equilibrium condition, (IV-1), (IV-3), and (IV-4) reduce to the equilibrium equations (IV-5), (IV-6) and (IV-7) respectively, using which the equilibrium values can be calculated.

$$\frac{K.(d+y_0).sin\,\theta_0}{(r^2+(d+y_0)^2-2.r.(d+y_0).cos\,\theta_0)^{3/2}} - mg\cos\theta_0 = r\frac{\theta_0}{C_m}, \qquad \text{(IV-5)}$$

$$\frac{K}{{x_0}^2}\frac{({x_0}^2+(d+y_0)^2-r^2)}{2x_0(d+y_0)} - \mu_s\left|\frac{Kr\sin\theta_0}{{x_0}^3}+mg\right| - k_{sp}y_0 = 0, \qquad \text{(IV-6)}$$

$${x_0}^2 = r^2 + (d+y_0)^2 - 2r(d+y_0)\cos\theta_0. \qquad \text{(IV-7)}$$

These models have been simulated and compared against the fixed-magnet system of Figure III-1, which corresponds to the spring constant k_{sp} value of infinity.

Minimum excitation amplitude to achieve bistability

An upper bound to the external vibration to achieve bistability can be found by computing the maximum vertical force experienced by the beam due to the combined effect of magnetic repulsion, mechanical compliance and the weight of the magnet on the cantilever tip. We find the angle θ_m and the spring compression y_m at which the vertical component of the force on the cantilever is maximized. The external force needed to achieve bistability must be weaker than this maximum vertical force since when the beam is in motion, even when the external force is weaker than one needed to overcome the maximum vertical force, the beam can continue to travel in the direction of the weaker excitation force owing to the kinetic energy of the moving beam. The aforementioned maximum vertical force experienced by the beam can be computed using a static analysis: this is the position where the excitation force needed to keep the beam in static equilibrium is maximized. In contrast, the position (θ_0, y_0) calculated earlier is where no excitation is needed to keep the beam in static equilibrium.

Referring to Figure IV-1 and (IV-1), the vertical force F_z at any given deflection angle θ, assuming static equilibrium, would consist of the vertical component of the magnetic force, $(K/x^2)\sin\alpha = Kr.\sin\theta/x^3$, the vertical component of the restorative force due to compliance, $(r\theta/C_m)\cos\theta$, and weight of the magnet on the cantilever tip, mg, as in (IV-8).

$$F_z = \frac{Kr\sin\theta}{x^3} - \frac{r\theta\cos\theta}{C_m} - mg \qquad \text{(IV-8)}$$

Recalling from (IV-4) that x is dependent on θ and y, we maximize (IV-8) with respect to θ and y such that the static case condition for the force acting on the spring-loaded magnet, given by (IV-9), derived from (IV-6), is satisfied.

$$k_{sp}y = \frac{K}{x^2}\frac{(x^2 + (d+y)^2 - r^2)}{2x(d+y)} \qquad \text{(IV-9)}$$

Identifying this as an optimization problem with dependent variables, we introduce a Lagrange multiplier λ, and rewrite the expression as (IV-10) to be maximized with respect to θ, y and λ.

$$\frac{Kr\sin\theta}{x^3} - \frac{r\theta\cos\theta}{C_m} - mg + \lambda\left[k_{sp}y - \frac{K}{x^2}\frac{(x^2+(d+y)^2-r^2)}{2x(d+y)}\right] \quad \text{(IV-10)}$$

Partially differentiating (IV-10) with respect to *θ*, *y* and *λ* and equating to zero, we get (IV-11) - (IV-13):

$$\frac{Kr}{x^3}(\cos\theta - 2\lambda\sin\theta) + \frac{3Kr(d+y)\sin\theta}{x^5}[\lambda(d+y-2r\cos\theta) - r\sin\theta] \quad \text{(IV-11)}$$

$$-\frac{r\cos\theta}{C_m} + \frac{r\theta\sin\theta}{C_m} = 0$$

$$\lambda\left(k_{sp} - \frac{K}{x^3}\right) + \frac{3K}{x^5}[r\sin\theta\{r\cos\theta - (d+y)\} \quad \text{(IV-12)}$$

$$+\lambda(d+y-2r\cos\theta)(d+y-r\cos\theta)] = 0$$

$$k_{sp}y - \frac{K}{x^3}(d+y-2r\cos\theta) = 0 \quad \text{(IV-13)}$$

Using the set of above three equations and (IV-4), we solve for θ_m, y_m and λ_m at which the vertical force F_z is maximized, and therefore find the maximum value of F_z. This maximum F_z is an upper bound to the excitation force required to overcome the magnetic force of repulsion, and hence push the cantilever into the bistable region of operation. It is expected that the minimum excitation force required to achieve a deflection to the zero angle (which corresponds to the boundary between the monostable and bistable behaviors) will approach the above upper bound as the excitation frequency is reduced, slowing down the beam and reducing the kinetic energy, and approaching the static condition. Table IV-1 lists the parameter values and the maximum vertical force F_z calculated for the spring constant value of $1*10^5$ N/m. All the other parameters are the same as the ones listed in Table III-1.

Table IV-1: Parameter values for the minimum excitation force required for bistable operation, for spring constant 1e5 N/m.

θ_m (radians)	y_m (mm)	λ_m	F_z (N)
0.0143	-1.0129	-0.0106	0.5337

Simulated and Experimental Results

Experimental setup

To validate our design ideas and models, we prototyped our harvester, shown in Figure IV-2. The setup is almost the same as was used in the case of the fixed-magnet harvester. It uses the same piezoelectric cantilever Volture V21B by Midé [47], and the bistability in the system is introduced using two permanent magnets (PMs) with same poles facing each other. However, in this case, the magnet opposite to the one on the cantilever is mounted on a spring and placed inside a cylindrical sleeve, so as to restrict its motion in the horizontal direction only. The output from the cantilever is again transferred to the battery through the extraction circuit built on a breadboard. The extraction circuits used were the same as those in the fixed-magnet case, with the component values listed in Table III-3, and the measurement setup was the same as the one shown in Figure III-17.

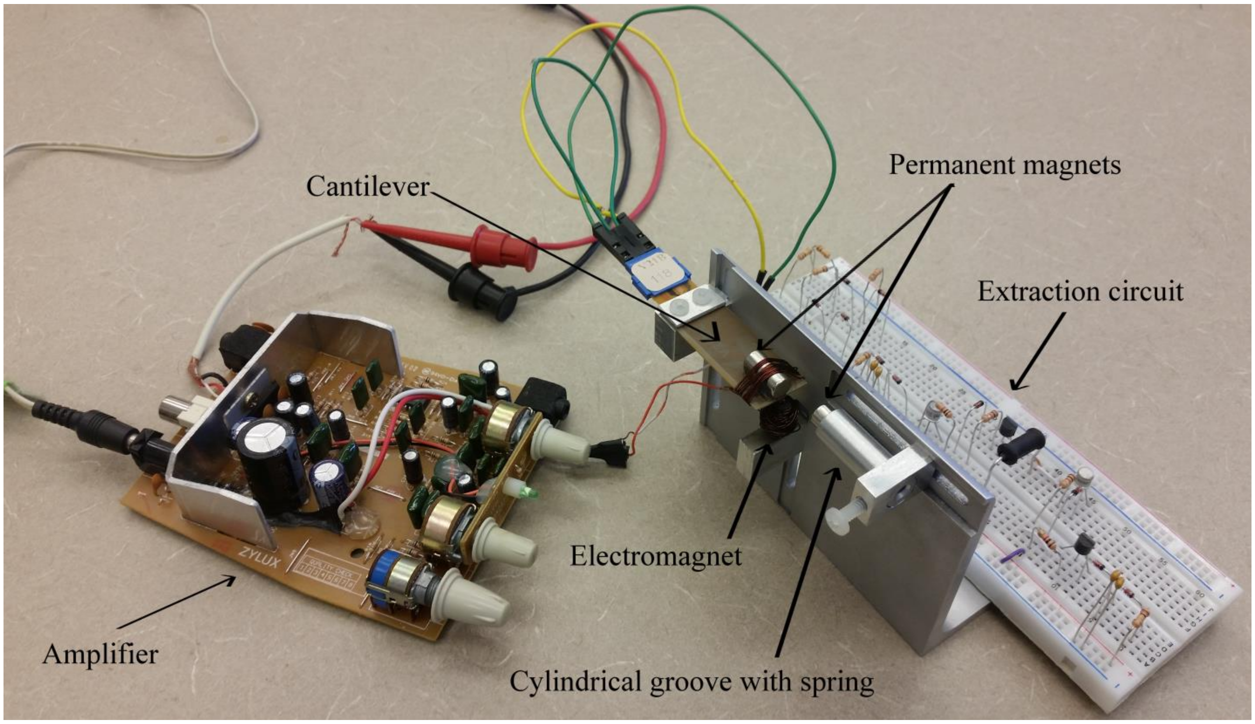

Figure IV-2: Experimental setup of the bistable harvester with spring-loaded magnet.

Results

The model for the bistable harvester with spring-loaded magnet was simulated in Matlab Simulink (Mathworks Inc.) [46], for a sinusoid input at 50 Hz and with a 300 kΩ resistive load. The parameter values used were the same as those listed in Table III-1. The *simulated* power outputs from systems with different spring constants, for varying excitation amplitudes, have been plotted in Figure IV-3. The simulations were performed under increasing amplitudes of the external vibration from 0.1V to 1V, and the power outputs were plotted for different values of the spring constant k_{sp} (N/m). In the plots, the excitation where the output power jumps up from very low values to high values represents the transition of the system from monostable to bistable operation. $k_{sp}=inf$ is the output plot for the system with the fixed PM, which exhibits bistable operation around 0.6N and above.

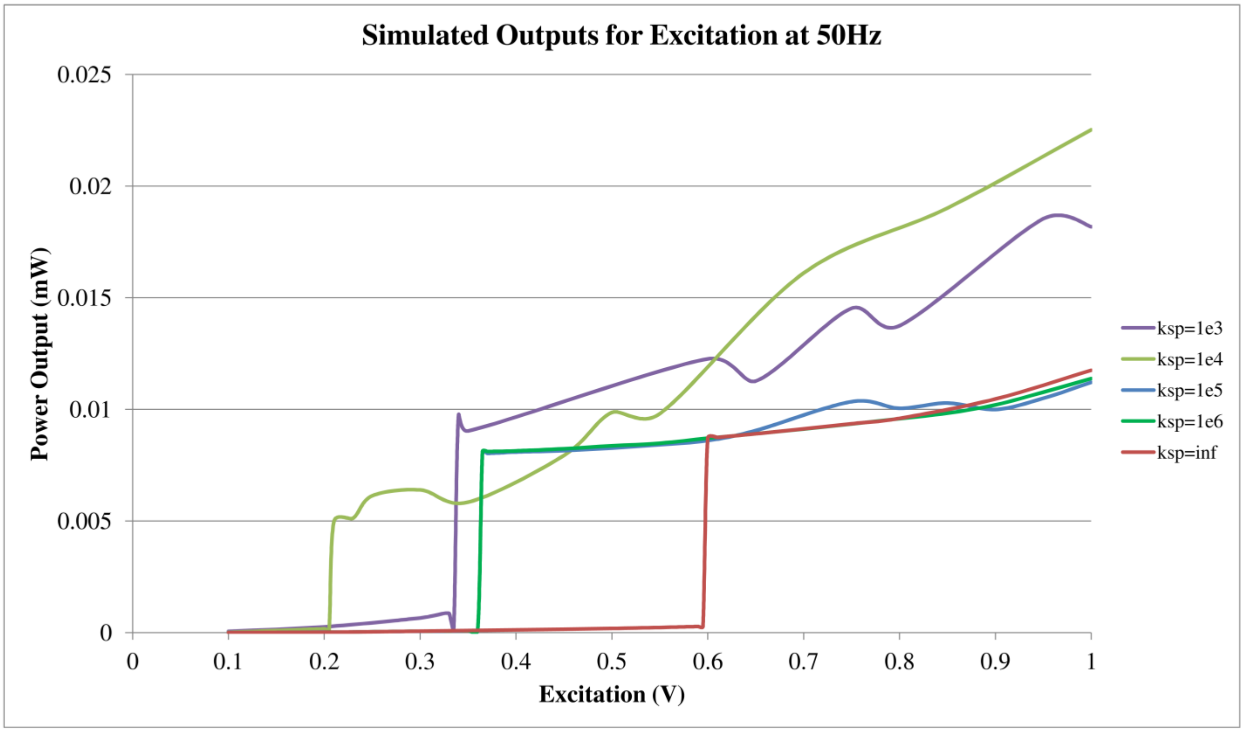

Figure IV-3: Simulated variation of power supplied to a resistive load of 300 kΩ with external vibration, for different spring constants.

From the plots, it is evident that for spring-loaded magnet systems, the system operates bistably at lower input excitations compared to the fixed PM system, indicating increased range of excitation over which the system remains bistable. The power output is also higher in the case of the spring loaded systems as compared to the fixed-magnet one. From Figure IV-3, we can conclude that depending on the range of input amplitudes of the application, a spring-loaded system with an appropriate value of spring constant k_{sp} may be chosen, maximizing the range over the given amplitudes that can activate bistability of operation.

Figure IV-4 shows the *experimental* power outputs for the same sinusoidal excitation at 50 Hz and 300 kΩ resistive load. Again, we can note the transition of the spring-loaded systems to the bistable mode at excitations lower than the fixed-magnet system, as well as the increased power output levels, thus validating our design ideas and models. While both simulated and experimental Figure IV-3 and Figure IV-4, respectively, show jump in output power at the excitation levels that can activate bistable operations, the simulated results (Figure IV-3) show slight fluctuation in output power as the excitation levels are continued to be raised, that is symptomatic of numerical stability issues – a race condition between the dynamics of the cantilever versus that of the spring-loaded magnet. Further, the effect of the race condition can be less pronounced in an actual implementation since a real spring does not respond instantaneously to the changes in the applied force, whereas the mathematical model assumes the spring to be ideal. However, the general trend is correct: that as input excitation is raised, so is the power output. Figure IV-5 shows the gains of the various spring constant systems over the fixed magnet system, and we can note gains of factor as high as 90, simply by the introduction of spring, that is a self-propelled negative feedback mechanism for automatically adjusting the distance between the two permanent magnets.

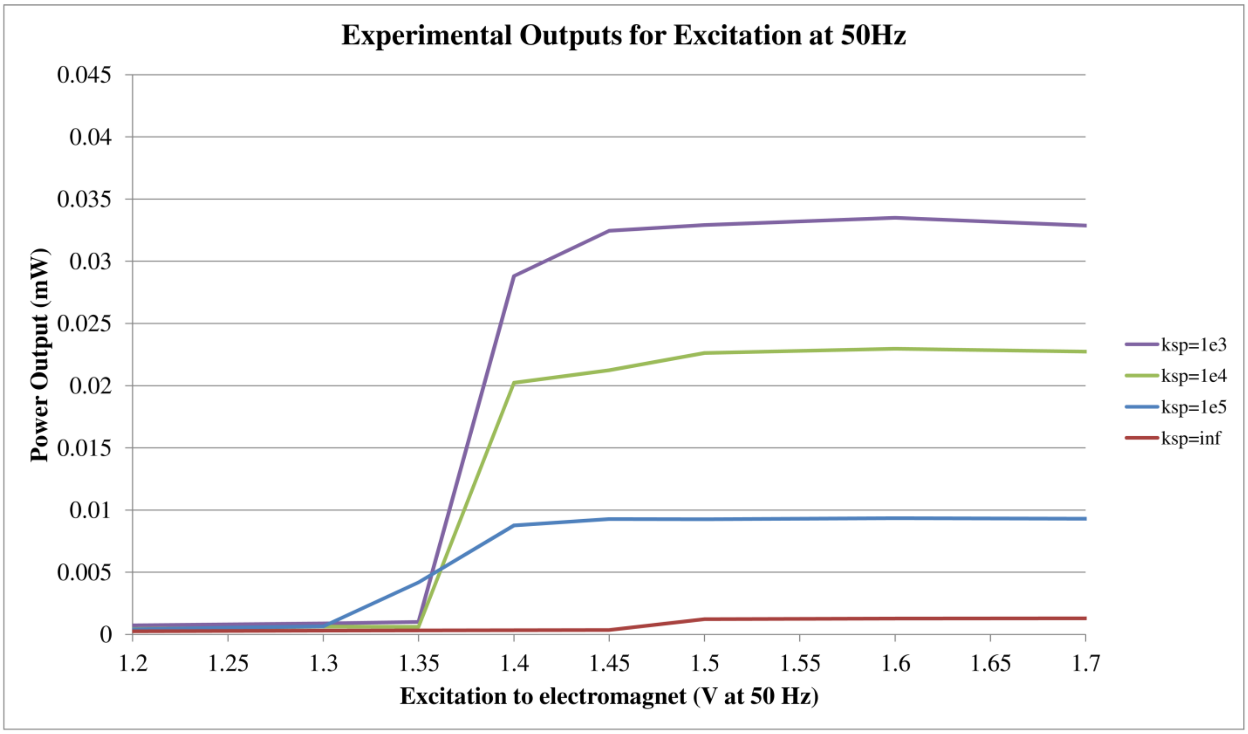

Figure IV-4: Experimental variation of power supplied to a resistive load of 300 kΩ with external vibration, for different spring constants.

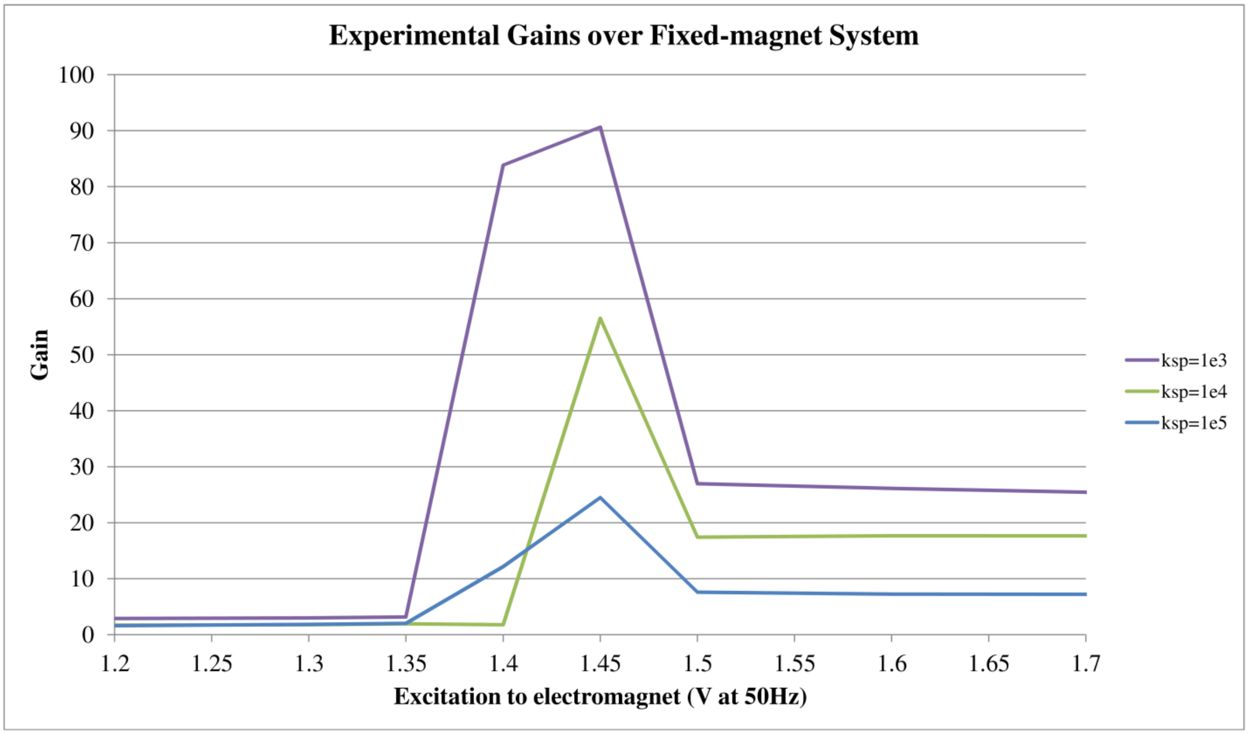

Figure IV-5: Experimental power gains of spring-loaded PM systems over fixed PM system.

The spring-loaded magnet systems were tested with the various extraction circuits mentioned in Chapter III, with a battery load at 90 Hz frequency. The power flowing into the battery at various excitations for different spring constant systems have been plotted for each extraction circuit in Figure IV-6 - Figure IV-8. For each of these circuits, we notice that for the range of excitations considered, the spring-loaded magnet systems not only lead to increased bistable range of operation, but comparable or higher power outputs. For example, considering the $k_{sp}=1*10^4$ *N/m* spring with the SCE circuit, we not only get a lowering of the cutoff for bistable activation of about 40 mV (a 33% reduction), the power output at 250 mV excitation almost doubles (100% increase) over that for the fixed magnet system, thus establishing a proof-of-concept for our design.

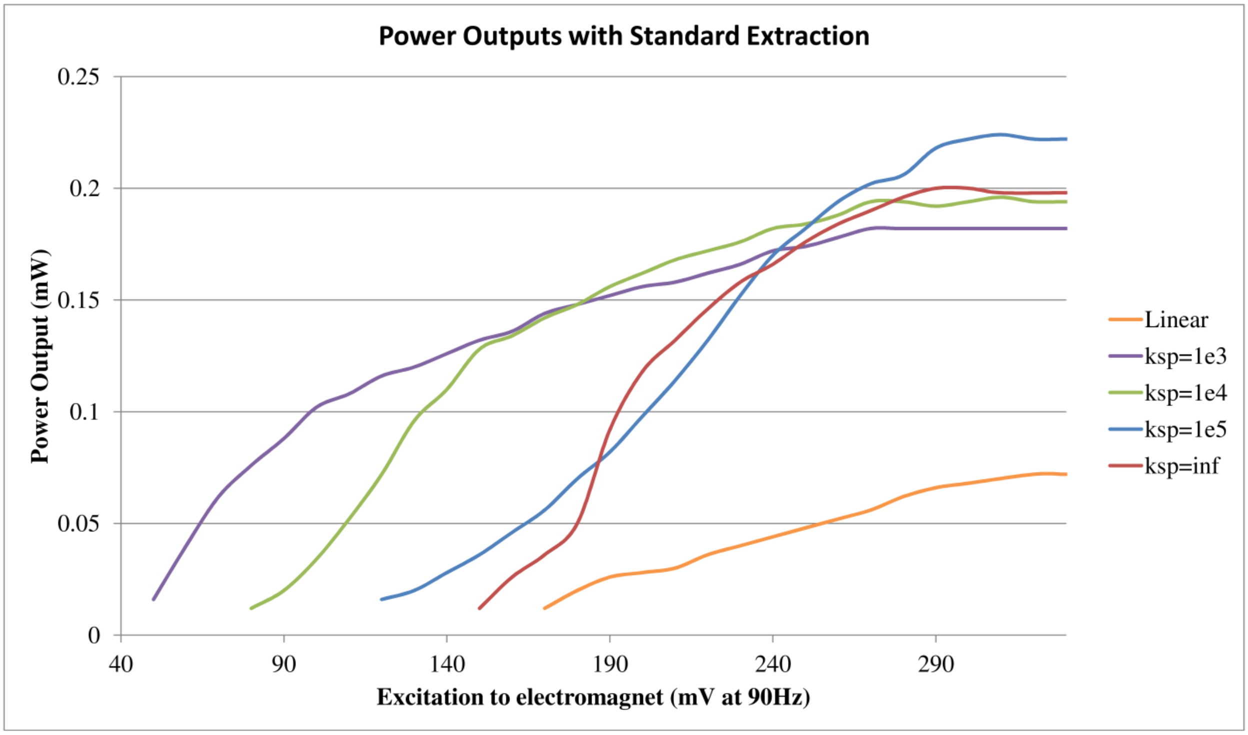

Figure IV-6: Power outputs of spring-loaded PM systems with standard extraction circuit.

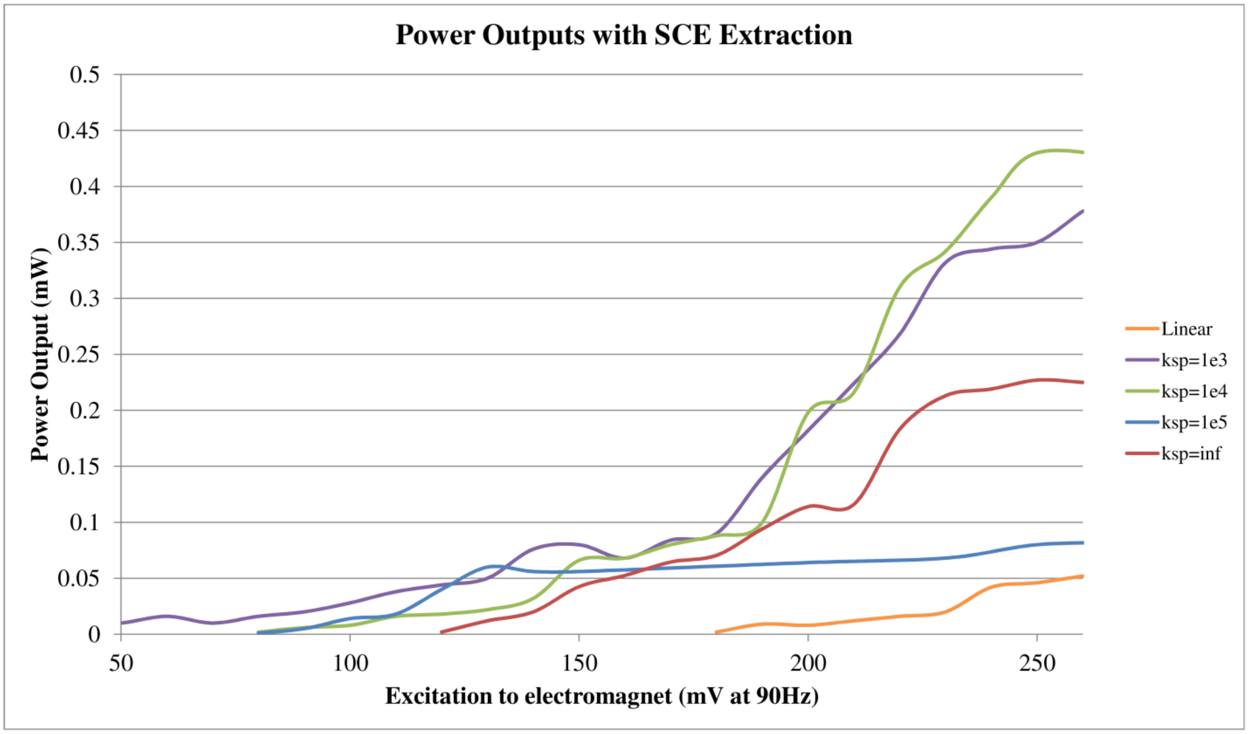

Figure IV-7: Power outputs of spring-loaded PM systems with SCE extraction circuit.

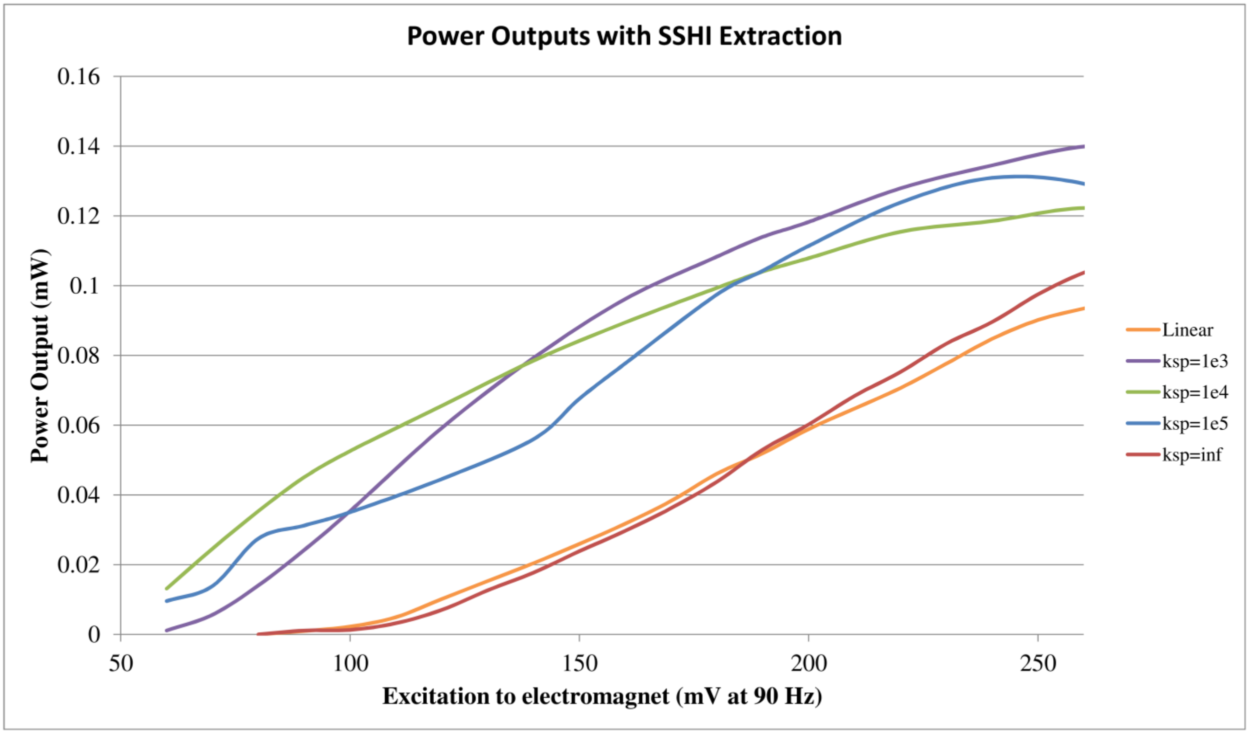

Figure IV-8: Power outputs of spring-loaded PM systems with SSHI extraction circuit.

In order to demonstrate the operation of the spring-loaded systems with broadband excitations, the multitone signal shown in Figure III-22 was used as input again, with frequencies varying from 1 to 95 Hz at 1 Hz intervals. The power outputs obtained for different spring constants, with the SSHI extraction circuit, have been plotted in Figure IV-9. Once again, the increased range of operation, and power output levels, for spring-loaded magnet systems over the fixed magnet one, is evident. For example, for $k_{sp}=1*10^5$ N/m system, we see an increase in power output by a factor of over 10% at higher excitation levels over the fixed magnet system, and lowering the cutoff for excitation by about 60 mV (a 60% reduction in the lower cutoff).

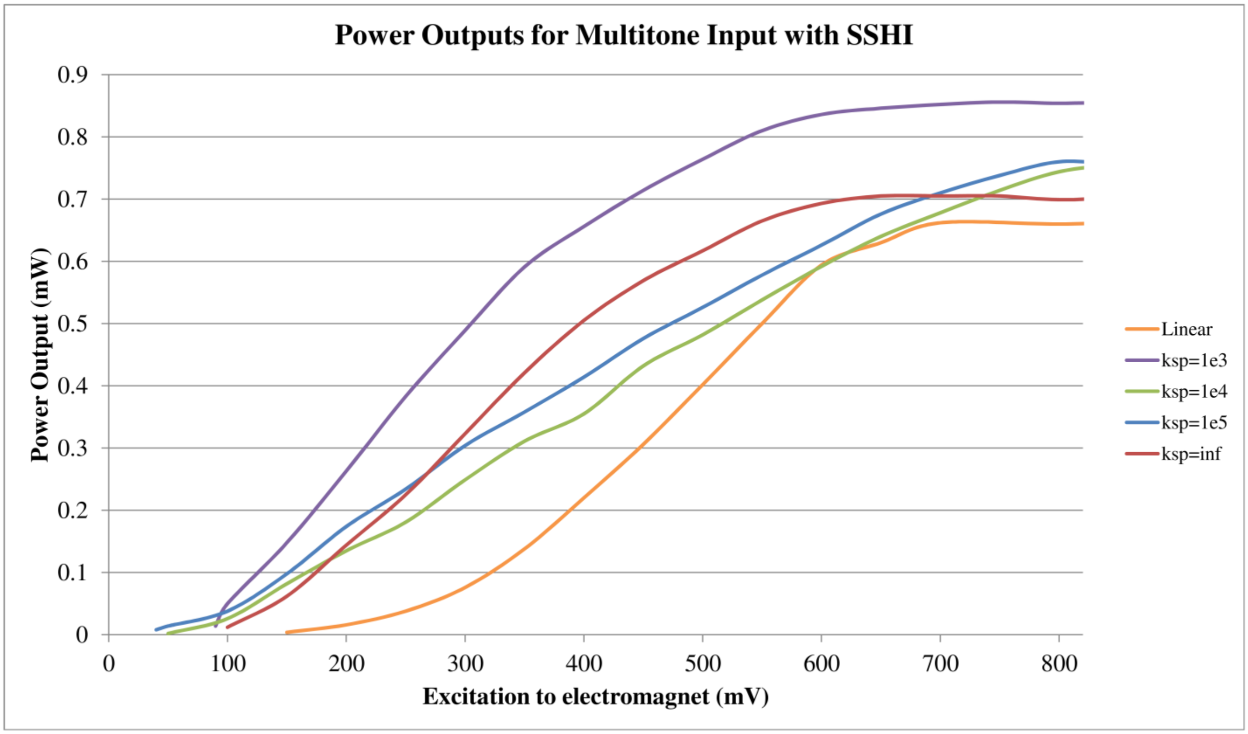

Figure IV-9: Power outputs of spring-loaded PM systems with SSHI extraction circuit for multitone input.

CHAPTER V

CONCLUSION, FUTURE DIRECTIONS, AND DISCUSSIONS

Conclusion

This work presented a nonlinear energy harvester for remotely located sensors, transducing energy from broadband ambient vibrations, e.g. thunder and structural vibrations. An accurate model of a nonlinear piezoelectric transducer was provided for a first time, augmenting the Butterworth van Dyke piezoelectric model, with the nonlinear input magnetic force acting as a nonlinear capacitor in a circuit analogy. The nonlinearity of the transducer was achieved through the use of repelling magnets. This nonlinear bistable transducer was then used with nonlinear SCE and parallel SSHI extraction. An electronic breaker was used as a self-propelled, low powered switch to detect extrema in the input and turn on and off automatically as required. Based on this work, the following observations were made:

- The nonlinearity of the transducer results in bistable behavior and increase of vibration amplitude, as well as the frequency spectrum of efficient operation. For the sinusoidal excitation of 1.63 N (acceleration of 500 m/s^2) at 10 Hz, using a 69.1 mm x 16.8 mm x 0.64 mm cantilever (piezoelectric dimensions 35.56 mm x 14.48 mm x 0.2 mm) manufactured by Midé, about 30% increases in the vibration amplitude and the open circuit piezoelectric voltage output were observed.
- The nonlinear synchronized extraction circuits lead to improved extraction of transduced power from the nonlinear transducer. For example:
    - For a sinusoidal vibration input of 0.146 N (acceleration of 45m/s^2) at 90 Hz, the harvested power from SCE and parallel SSHI circuits were experimentally

determined to be respectively, 320.24 µW and 385 µW, with respective gains of 1.85 and 2.23 over the linear transducer with standard extraction circuit.

- These gains increase significantly to 34.25 and 9.14 respectively for nonlinear bistable operation when the input excitation is a broadband multitone.
- Gains over a factor of 100 were also observed over some of the reported harvested power in literature.

These gains result from the inclusion of nonlinearity in the form of bistable mode operation, combined with the synchronized circuits for energy extractions. To the best of our knowledge, this combination is the first reported in literature.

The next part of the work presented a completely mechanical way of adjusting the distance between the magnets of the bistable piezoelectric vibration energy harvester, thus adjusting the magnetic force of repulsion in response to the applied excitation, so as to increase the excitation amplitude range over which the harvester operates in the bistable mode. Spring-loading the previously fixed magnet introduces implicitly a negative feedback: as the magnet at the tip of cantilever approaches the spring-loaded magnet, the spring compresses, increasing the distance between the magnets, and vice-versa. Again, the following observations were made:

- Spring-loading the magnet leads to not only increased input amplitude range of bistable operation, but also increased power output levels.
- Increased efficiency, with power gains of up to 90% over the fixed magnet system, was demonstrated for sinusoidal excitation at 50 Hz across a 300 kΩ resistor.
- For 90 Hz excitation frequency with an SCE circuit and a battery as load, lowering of the cutoff for bistable activation by up to 40 mV of excitation was noted (a 33% reduction), with power level increase of about 100%.

- For a broadband multitone input with an SSHI extraction circuit with a battery as load, lowering of the cutoff for bistable activation by about 60 mV was observed (about 60% reduction) with up to 20% power level increase.

The output plots shown for different spring constants indicate that depending on the range of input amplitudes of the application, a spring-loaded system with an appropriate value of spring constant may be chosen so the activation of the bistable mode can occur at the lowest excitation. Also, this work has been presented as a proof of concept, and the various parameters can be adjusted according to the specifications of a desired application for improved harvesting.

Future Directions

There is scope for using this work in various applications, as well as using it as a basis and extending it in further directions. Some of these have been identified below:

- Derivation of an optimized value of spring-constant for a given distribution of ambient excitation would be an interesting analytical work for future development. We have performed some initial calculations, presented in Chapter IV, to find the minimum excitation amplitude required to overcome the magnetic repulsive force in the static case, given the magnetic force and the spring constant. This work could be extended to the dynamic case when the cantilever is in motion, for which, the required force would be less than that in the static case. Using this information, for a given excitation and the magnetic force used, we can find the value of the spring constant for which the performance of the harvester is optimized.
- Based on the above information, as well as by adjusting the parameters of the piezoelectric cantilever presented in Table III-1, the vibration energy harvester could be

customized for various applications, including structural health monitoring sensors like bridge sensors, energy harvesting from vehicular vibrations, thunder, human motion, and so on.

- Using the power requirement data for a typical bridge sensor presented in [7], and assuming the sensor operates for sixty (60) minutes in a day, the average power consumption by the sensor over a 24 hour period can be calculated to be 3.68 mW. Typical bridge vibrations tend to have very low accelerations of 0.1-1 m/s^2 over a frequency band of about 1-40 Hz [8]. For a similar excitation with accelerations of 0.1-1 m/s^2 at 20 Hz, we were able to customize the parameters of our nonlinear bistable spring-loaded harvester in simulations, using a spring of spring constant 1x10^6 N/m, to achieve an average power output of 1.105 mW, which provides about 30% of the power requirements of a typical bridge sensor.
- Considering a 1 GJ lightning stroke, and assuming a one percent acoustic conversion, it produces about 10 MJ of acoustic energy. For a strike at the nominal height of 1 km from the ground, and assuming spherical expansion of the acoustic wave, about 0.8 J/m^2 of energy reaches the ground surface. Since the reflection coefficient at the air-soil interface is large due to difference in densities (power reflection coefficient of about 0.996), only 0.4% of the wave energy penetrates the ground, with only about 1 dB attenuation up to a depth of 1 m [56]. Hence, about 3.2 mJ/m^2 of energy is available to the ground. Assuming efficient coupling, for a transducer of dimensions similar to Volture V21B by Midé used in our experiments, the energy transduced would be about 3.7 μJ. The above discussion is based on calculations performed by Weber [57].

- Another possible direction for future research might be to look for methods of harvesting from other ambient sources, and integrate those with the bistable piezoelectric vibration energy harvester, so as to have a more universal harvester, capable of harvesting from multiple available ambient sources. Some of these sources, such as light, wind, fuel cells and biogas, have been discussed in the following section.
- Other possible harvesting domains could be explored where nonlinear synchronized extraction could be used for better efficiency, especially for source nonlinearity, and possibly for source variability. Besides vibration, these might include harvesting from tidal waves, human motion, vehicular motion, and even possibly wind energy.
- In order to charge batteries from the harvester, a power conditioner circuit, such as constant current/constant voltage charging, might be looked into, so as to prevent overcharging or over-currents, which might set the battery on fire. If current levels are low due to the low power levels involved, power conditioning might not be required, in which case some method can be developed to shut off charging when the battery is full.
- As an improvement to the extraction circuits, synchronous rectification with switches could be employed in order to eliminate power losses due to the diodes.

Discussions

A review of maximum power point tracking methods

Some other ambient energy sources which were studied in the course of this research were light, wind, fuel cells, and biogas. Most of these systems operate optimally under a particular set of conditions, called the maximum power point (MPP). In order to locate and operate at this MPP, they employ various maximum power point tracking (MPPT) methods. The purpose of this study was to review the various MPPT methods employed for different ambient sources.

Photovoltaic systems

The output from a photovoltaic (PV) array varies throughout the day with the variation of temperature and solar radiation [58]. The characteristic curves have been shown in Figure V-1 [58], and can be used to understand the principle of MPPT. The line with slope $1/R_0$ represents a constant load R_0, corresponding to operation at power P_a, while the maximum power which can be obtained is observed to be P_b. Therefore, a power converter is introduced in between the PV array and the load, so as to alter the load characteristics to match the MPP operation. In the figure, D^2/R_0 is the transformed load seen by the PV array when a step down converter with duty cycle D is used.

Various methods have been developed for MPPT in PV systems [58-61]. The hill-climbing or perturb-and-observe methods [59] involve perturbing the duty ratio of the power converter so as to change the PV array current, and hence the voltage, and observing the change in power output. As can be seen from Figure V-2, incrementing (resp. decrementing) the voltage when operating on the left of the MPP increases (resp. decreases) the power, and decreases (resp. increases) it when operating on the right of the MPP. Thus, if an increase in power is observed, the perturbation should be kept the same till the MPP is reached, while if the power decreases, the perturbation should be reversed. Once the MPP is reached, the system oscillates around it.

Another method, the incremental conductance method, makes use of the fact that the slope of the power characteristic curve, dP/dV, is zero at the MPP, positive to the left of it, and negative to the right [59]. Since $dP/dV = d(VI)/dV = I + VdI/dV \approx I + V\Delta I/\Delta V$, the characteristics of the slope could be reformulated in terms of the instantaneous conductance I/V and the incremental conductance $\Delta I/\Delta V$, such that $\Delta I/\Delta V = - I/V$ at MPP, $\Delta I/\Delta V > - I/V$ on the left of MPP, and $\Delta I/\Delta V < - I/V$ on the right. Thus, comparing the instantaneous and incremental conductances, the voltage can be adjusted till the MPP is reached, at which point the operation is maintained unless a change in ΔI is noted, indicating a change in atmospheric conditions, and hence the MPP.

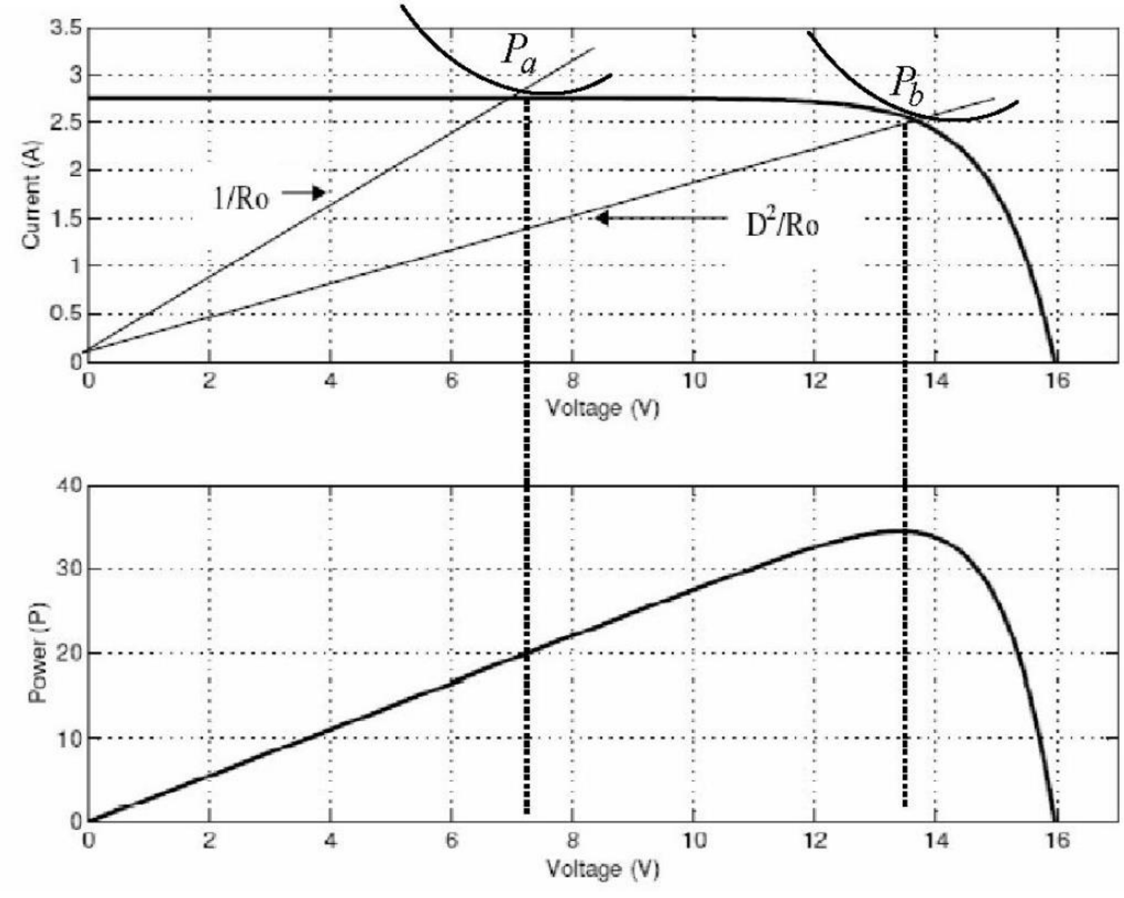

Figure V-1: Characteristic curves for PV array, as shown in [58].

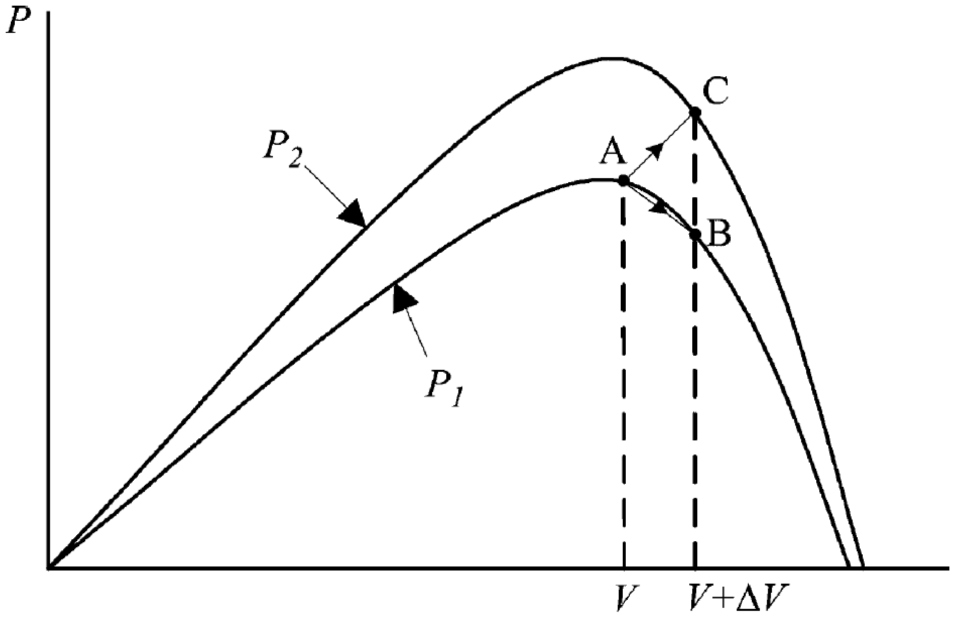

Figure V-2: Divergence of perturb and observe from MPP, as shown in [59].

A number of similar algorithms based on the power characteristic curve, such as fuzzy logic control, ripple correlation control, and *dP/dV* or *dP/dI* feedback, have been developed [59].

Wind energy

As in the case of a PV array, the power captured P_w by a wind generator (WG) varies based on a number of factors, as given in (V-1) [62]:

$$P_w = \frac{1}{2}\pi\rho_w C_{pw} R_w^2 V_w^3 \tag{V-1}$$

where ρ_w is the air density, C_{pw} is the wind-turbine power coefficient, R_w is the blade radius, and V_w is the wind speed. C_{pw} is itself dependent on the blade pitch angle and the tip speed ratio $\lambda_w = \Omega_w R_w / V_w$, where Ω_w is the WG rotor speed. The WG power coefficient, and hence the power captured, is maximized for a constant tip-speed ratio value λ_{opt}. As is seen from Figure V-3, for each wind speed V_n, there exists a particular WG speed $\Omega_n = \lambda_{opt} * V_n / R_w$ for which the WG power is maximized. The MPPT control in this case involves changing the WG load, once again by employing a power converter, so as to bring the operating point to the optimum Ω_n value.

The equivalent circuit of a generator is shown in Figure V-4, where $E_A = K_m\phi\Omega_w = V_\phi + jX_sI_A + R_AI_A$ is the generated electromotive force, K_m being the machine constant and ϕ the magnetic flux. X_s is the stator leakage reactance, R_A is the armature resistance, I_A is the armature current, and V_ϕ is the terminal phase voltage. From the above relation, Ω_w can be expressed as in (V-2), which indicates that Ω_w can be adjusted by controlling V_ϕ.

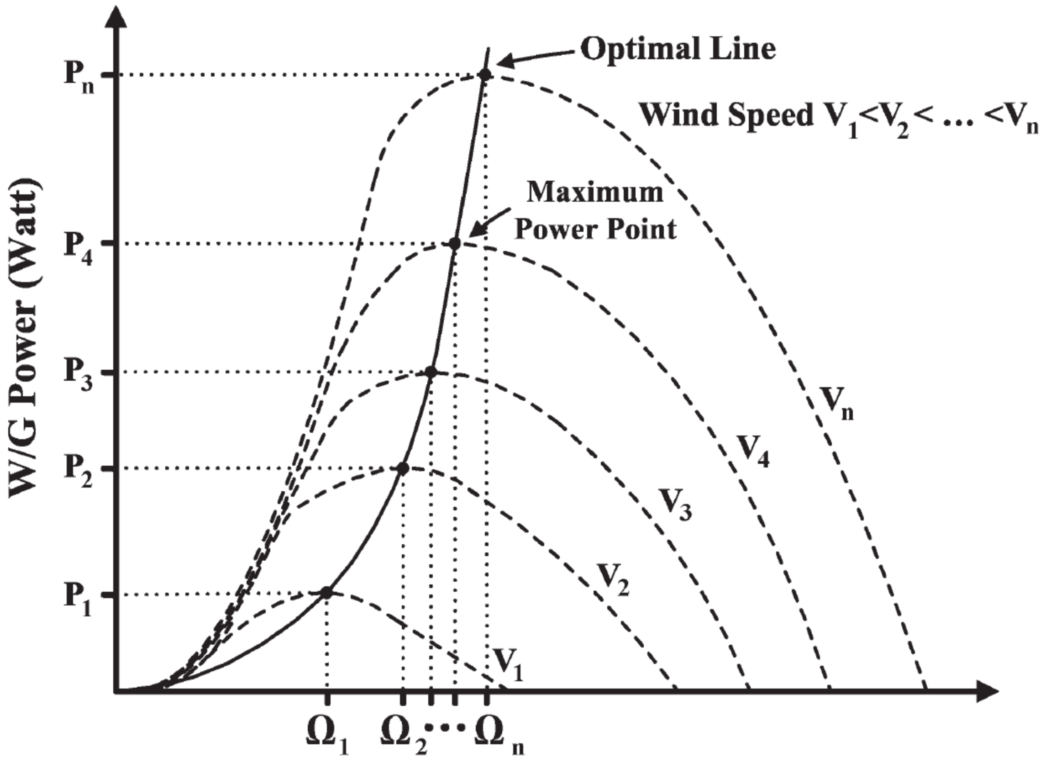

Figure V-3: WG power characteristic curves at various wind speeds, as shown in [62].

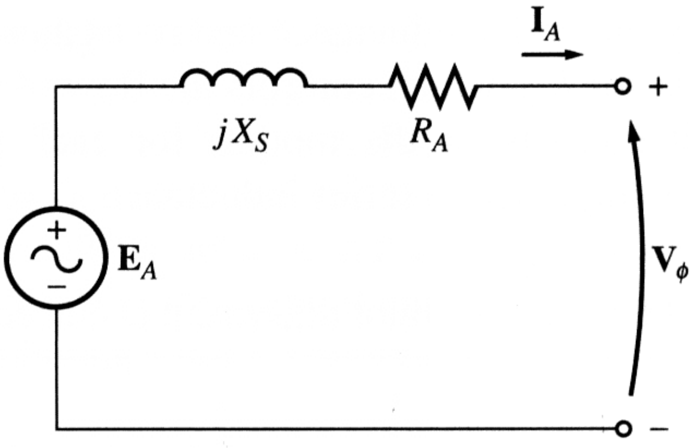

Figure V-4: Equivalent model of a wind generator.

$$\Omega_w = \frac{V_\phi + jX_s I_A + R_A I_A}{K_m \phi} \tag{V-2}$$

For the wind generator converter system shown in [63] and reproduced here in Figure V-5, the DC link voltage, V_{DC}, is directly proportional to V_ϕ, and hence Ω_w can be controlled by controlling V_{DC} with the help of a power converter.

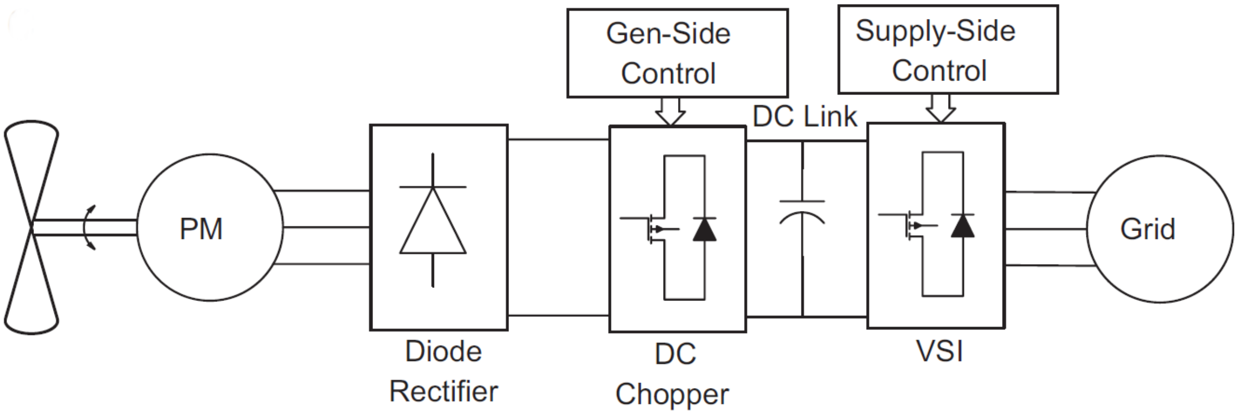

Figure V-5: Wind generator converter model, as shown in [63].

A number of different methods have been developed for maximum power point tracking for wind generators [62-68]. The MPPT method presented in [62] makes use of the fact that at the MPP, the slope $dP/d\Omega_w = 0$. This condition can be rewritten as $dP/d\Omega_w =$

$(dP/dD)*(dD/dV_{WG})*(dV_{WG}/d\Omega_w) = 0$, where D is the duty cycle of the power converter, and V_{WG} is the rectifier output voltage level. The MPPT process is shown in Figure V-6. Noting that the duty-cycle adjustment follows the direction of dP/dD, increasing D on the right of MPP results in the reduction of WG rotor speed, and hence power increase, till MPP is reached. Similarly on the left of MPP, reducing the duty cycle leads to increased power outputs till MPP is reached. The perturb-and-observe method used for PV systems can be employed here as well to reach MPP.

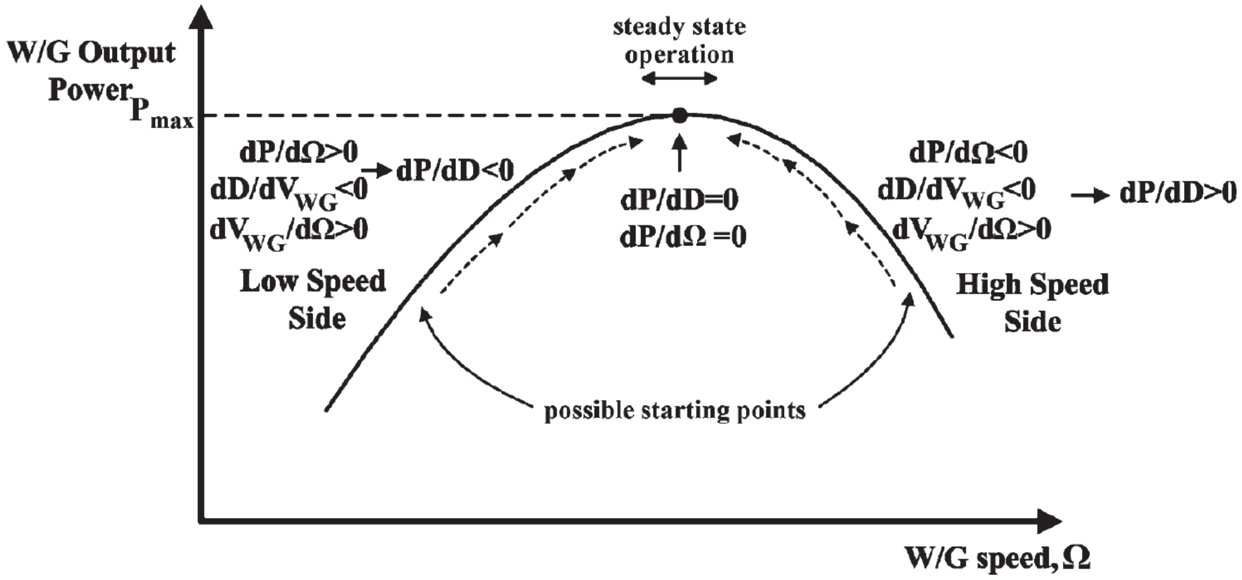

Figure V-6: WG MPPT process, as shown in [62].

Authors in [62] use a DC-DC power converter to optimally charge a battery by adjusting the duty cycle of the converter, and hence the phase voltage and the generator speed, as shown in Figure V-7. Since this is similar to extracting the maximum amount of power from a generator, as in the case of the power extraction circuits used with the nonlinear bistable vibration energy harvester above, it may be conjectured that a system with a capacitor introduced after the rectifier in Figure V-7, and replacing the DC-DC converter with the synchronous charge extraction (SCE) circuit, might work as an MPPT technique. This power extraction scheme for wind generation could be studied as future work, to see if nonlinear synchronous extraction circuits could be used for optimally charging a battery. The consequences of being able to use such a scheme would be significant, since the SCE circuit is an automatically switched circuit which would eliminate the need of any current and voltage sensing, and hence the need of any feedback in the currently used MPPT techniques.

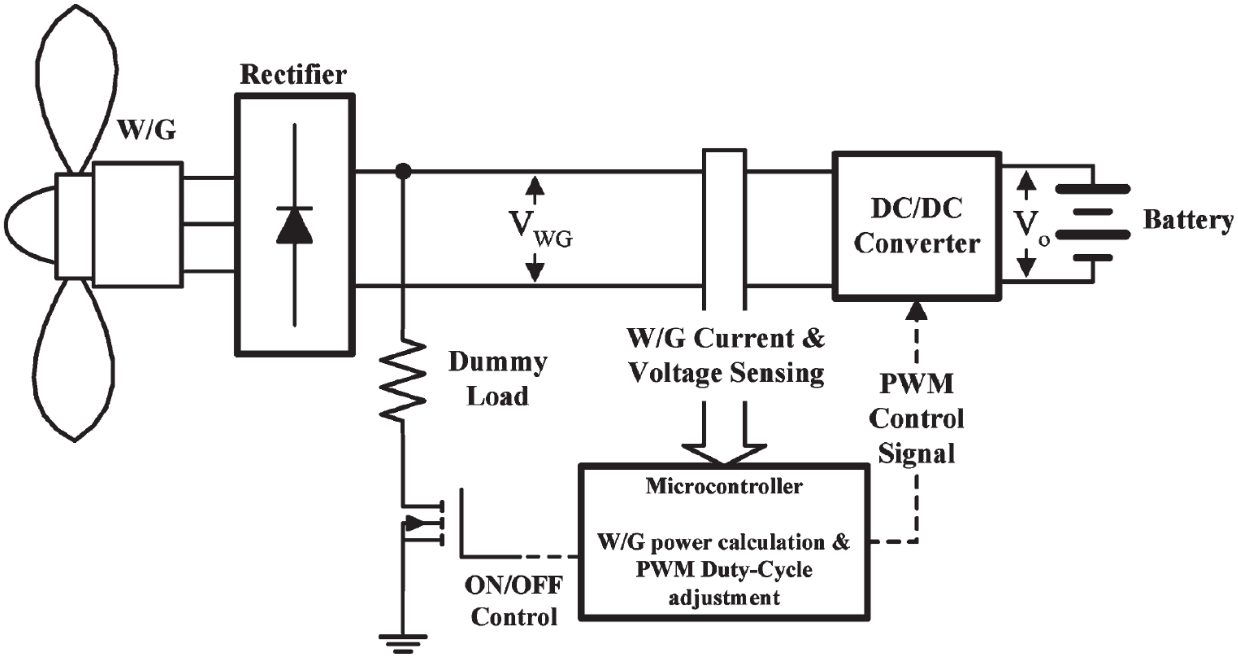

Figure V-7: Block diagram of the MPPT system used in [62].

Some other MPPT methods involve knowledge of the WG optimal power versus the rotating speed characteristics, which is stored in the microcontroller memory [62]. Based on this information, the WG rotating speed is measured, the optimal output power is calculated and compared to the actual power output, and the resulting error is used to control the power converter. Similarly, the WG output power may be measured and the target rotor speed found from the optimal characteristic curve, which is then compared to the actual rotor speed and the error used for power converter control. Another similar method involves measurement of the wind speed to calculate the optimal rotor speed, which is then compared to the actual rotor speed, and the error used for control. As an example, authors in [66-68] plot the optimum DC voltage, current, and power at every shaft rotational speed, and use this information to calculate the optimal values of the power angle and the inverter AC voltage magnitude. The power angle is then controlled by timing the switches in the inverter, while the inverter AC voltage magnitude is controlled through the modulation index of the inverter, or by using a DC-DC converter to maintain a constant DC-link voltage.

Fuel cells

The output power from a fuel cell depends both on the internal electro-chemical reaction and the external load impedance. Different works have focused on different factors in order to maximize the power drawn from a fuel cell [69-72].

As shown in Figure V-8, there exists a unique MPP at which the fuel cell produces maximum power. Similar to the perturb-and-observe method introduced earlier, authors in [69] use a power converter and perturb its duty cycle so as to adjust the equivalent load impedance, and hence the operating current, and observe the output to achieve the optimum operating point.

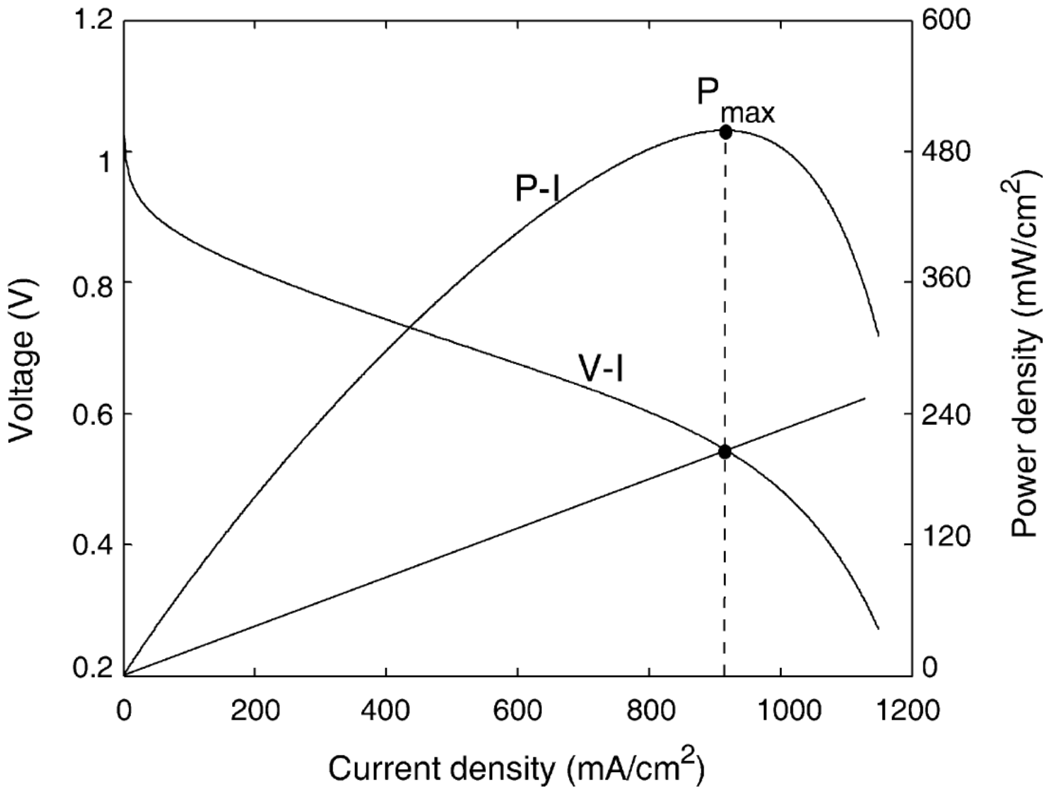

Figure V-8: Typical fuel cell polarization and power characteristic curves, as shown in [69].

Other MPPT methods for fuel cells include the extremum seeking approach described in [70] where the motor voltage of the compressor supplying air to the fuel cell is perturbed to adjust the air supply, and hence the oxygen excess ratio, defined as the ratio of the mass flow rates of oxygen entering the cathode and of that being consumed by the reaction. From Figure V-9, it is evident that the power output from a fuel cell is maximized for a particular value of the oxygen excess ratio. Thus perturbing the motor compressor voltage, the oxygen excess ratio corresponding to the MPP is sought.

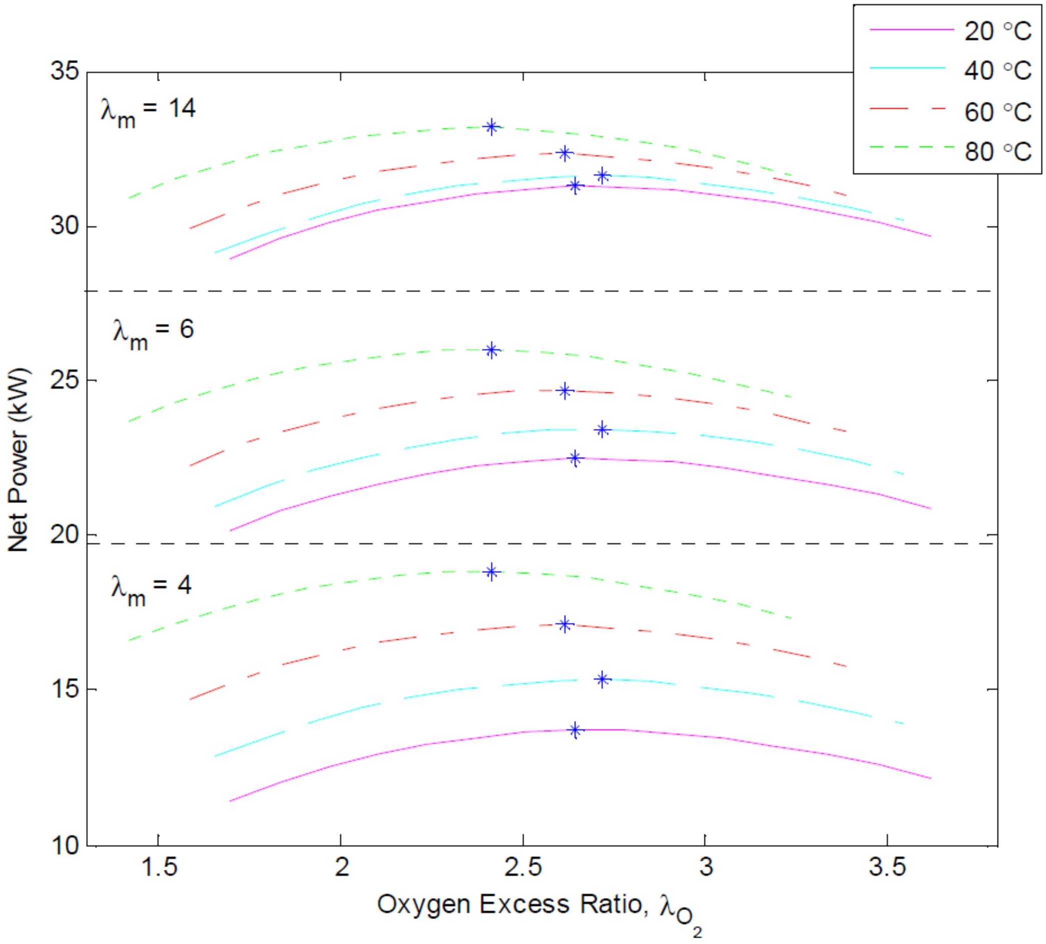

Figure V-9: Fuel cell power curves with respect to oxygen excess ratio, as shown in [70].

Biogas systems

Studies in biogas systems include methods to optimize biogas production, such as artificial neural networks to predict the production of methane based on inputs like temperature, pH, total solids, volatile solids, etc., and genetic algorithms to find the maximum output of methane and the combination of inputs to achieve it [73]. Authors in [74] present a renewable energy distributed power system by integrating a wind generator with a biogas generator, and use the latter to balance the output power of the system, controlling the biogas generator output by adjusting the mass input of biogas into the generator, in order to produce the required power.

Effects of scaling

MEMS fabrication offers a low-cost method of developing miniature bistable piezoelectric vibration energy harvester presented in this work. However, the performance of piezoelectric-based vibration energy harvesters is dependent on the dimensions of the harvester. Scaling the piezoelectric material affects the power output and the excitations at which the harvester performs efficiently, as has been shown in [75]. At constant vibration accelerations, the maximum output power which is transduced by the harvester is proportional to fourth powers of the scaling factor, while it remains unchanged when excited under constant vibration amplitudes. Hence, scaling down the harvester reduces the power output. Further, the resonant frequency increases as the cantilever is scaled down, and vice versa. From our discussion on the frequency dependence of harvester performance, we can surmise that scaling down the harvester would result is efficient performance at higher frequencies.

REFERENCES

[1] G. Pandey, R. Kumar, R.J. Weber, “Real Time Detection of Soil Moisture and Nitrates using On-board In-situ Impedance Spectroscopy”, *IEEE Int. Conf. Syst., Man, Cybernetics, Manchester, UK*, 2013.

[2] G. Pandey, R. Kumar, R.J. Weber, “A Multifrequency, Self-Calibrating, In-situ Soil Sensor with Energy-Efficient Wireless Interface”, *Defense, Sensing and Security Conf., SPIE, Baltimore, MD*, 2013.

[3] G. Pandey, R. Kumar, R.J. Weber, “A Low RF-band Impedance Spectroscopy based Sensor for In-situ, Wireless Soil Sensing”, *IEEE Sensors J.*, Vol. 14., No. 6, pp. 1997-2005, June 2014.

[4] G. Pandey, R. Kumar, R.J. Weber, “Design and Implementation of a Self-calibrating, Compact Micro Strip Sensor for In-situ Dielectric Spectroscopy and Data Transmission”, *IEEE Sensors Conf., Baltimore*, 2013.

[5] G. Pandey, R. Kumar, R.J. Weber, “Determination of Soil Ionic Concentration using Impedance Spectroscopy”, *Defense, Sensing and Security Conf., SPIE, Baltimore, MD*, 2013.

[6] G. Pandey, R. Kumar, R.J. Weber, “A Low Profile, Low-RF Band, Small Antenna for Underground, In-situ Sensing and Wireless Energy-Efficient Transmission,” *IEEE 11th Int. Conf. Networking, Sens., Ctrl., Miami, FL*, Apr. 2014.

[7] A. M. Hedayetullah, “Analysis of Piezoelectric Energy Harvesting for Bridge Health Monitoring Systems,” M.S. Thesis, University of Wales Swansea, 2010.

[8] T. Galchev, J. McCullagh, R.L. Peterson, K. Najafi, “Harvesting Traffic-Induced Bridge Vibrations,” *16th Int. Solid State Sens. Act. Microsyst. Conf. (TRANSDUCERS)*, pp. 1661-1664, 5-9 Jun 2011.

[9] T. Galchev, J. McCullagh, R.L. Peterson, K. Najafi, “A Vibration Harvesting System for Bridge Health Monitoring Applications,” *PowerMEMS*, Leuven, Belgium, pp. 179-182, 2010.

[10] C.B. Williams, R.B. Yates, “Analysis of a Micro-electric Generator for Microsystems," *Solid-State Sens. and Acts., 1995 and Eurosensors IX. Transducers '95. The 8th Int. Conf.*, Vol.1, pp. 369-372, 25-29 Jun 1995.

[11] S.P. Beeby, M.J. Tudor, N.M. White, “Energy Harvesting Vibration Sources for Microsystems Applications,” *Measurement Science and Technology*, Vol. 17, No. 12, pp. R175-R195, Jul 2006.

[12] V. Smil, “Power Density Primer: Understanding the Spatial Dimension of the Unfolding Transition to Renewable Electricity Generation,” URL: http://www.vaclavsmil.com/wp-content/uploads/docs/smil-article-power-density-primer.pdf, last accessed Nov. 18, 2015.

[13] Biomass Energy Centre, Typical calorific values of fuels, URL: http://www.biomassenergycentre.org.uk/portal/page?_pageid=75,20041&_dad=portal&_schema=PORTAL, last accessed Nov. 18, 2015.

[14] A. Perez-Rodriguez *et al.*, "Design of Electromagnetic Inertial Generators for Energy Scavenging Applications," *Proc. Eurosensors XIX (Barcelona, Spain),* paper MC5, 2005.

[15] S.P. Beeby *et al.*, "Micromachined Silicon Generator for Harvesting Power from Vibration," *Proc. Transducers (Seoul, Korea),* pp. 780-783, 2005.

[16] M. El-Hami *et al.*, "Design and Fabrication of a New Vibration-based Electromechanical Power Generator," *Sens. Act. A: Phys.* Vol. 92, pp. 335-342, 2001.

[17] P. Glynne-Jones, M.J. Tudor, S.P. Beeby, N.M. White, "An Electromagnetic, Vibration-powered Generator for Intelligent Sensor Systems," *Sens. Actuat. A: Phys.*, Vol. 110, pp. 344-349, 2004.

[18] S. Meninger *et al.*, "Vibration to Electric Energy Conversion," *IEEE Trans. VLSI Syst.*, Vol. 9, pp. 64-76, 2001.

[19] G. Despesse *et al.*, "Fabrication and Characterization of High Damping Electrostatic Micro Devices for Vibration Energy Scavenging," *Proc. Design, Test, Integ. Pack. MEMS & MOEMS*, pp. 386–390, 2005.

[20] R. Tashiro *et al.*, "Development of a Electrostatic Generator for a Cardiac Pacemaker that Harnesses the Ventricular Wall Motion," *J. Artif. Organs*, pp. 239-245, 2002.

[21] P. Mitcheson *et al.*, "Analysis and Optimization of MEMS Electrostatic On-Chip Power Supply for Self Powering of Slow-Moving Sensors," *Proc. Eurosensors XVII (Guimaraes, Portugal),* pp. 48-51, Sept. 2003.

[22] M. Umeda, K. Nakamura, S. Ueha, "Analysis of the Transformation of Mechanical Impact Energy to Electric Energy using Piezoelectric Vibrator," *Japan. J. Appl Phys.* Vol. 35, pp. 3267-3273, May 1996.

[23] M. Umeda, K. Nakamura, S. Ueha, "Energy Storage Characteristics of a Piezo-generator using Impact Induced Vibrations," *Japan. J. Appl. Phys.*, Vol. 36, pp. 3146-3151, May 1997.

[24] N.S. Shenck, J.A. Paradiso, "Energy Scavenging with Shoe-Mounted Piezoelectrics," *IEEE Micro,* Vol. 21, No. 3, pp. 30-42, May/Jun 2001.

[25] S. Roundy, P.K. Wright, "A Piezoelectric Vibration Based Generator for Wireless Electronics," *Smart Mater. Struct.*, Vol. 13, pp. 1131-42, 2004.

[26] H. Li, A. Lal, "Self-Reciprocating Radioisotope-Powered Cantilever," *J. Appl. Phys.*, Vol. 92, No. 2, pp. 1122-1127, Jul. 2002.

[27] J. Huang, R.C. O'Handley, D. Bono, "New, High-Sensitivity, Hybrid Magnetostrictive/Electroactive Magnetic Field Sensors," *SPIE 5050, Smart Struc. Mat.: Smart Sens. Tech. Meas. Syst.*, pp. 229-237, 2003.

[28] S. Roundy, "On the Effectiveness of Vibration-based Energy Harvesting", *J. Intel. Mat. Syst. Struc.*, Vol. 16, pp. 809-823, Sep. 2005.

[29] K.A. Singh, R. Kumar, R.J. Weber, "Piezoelectric-based Broadband Bistable Vibration Energy Harvester and SCE/SSHI-based High-Power Extraction," *IEEE 11th Int. Conf. Networking, Sens., Ctrl., Miami, FL*, pp. 197-202, Apr. 2014.

[30] K. A. Singh, R. Kumar, R. J. Weber, "A Broadband Bistable Piezoelectric Energy Harvester with Nonlinear High-Power Extraction," *IEEE Trans. on Power Electronics*, Vol. 30, No. 12, pp. 6763-6774, Dec. 2015.

[31] K. A. Singh, R. Kumar, R. J. Weber, "A Self-propelled Mechanism for Increasing Bistable Range of Operation of a Piezoelectric Cantilever based Vibration Energy Harvester," *IEEE Trans. on Power Electronics*, submitted Oct. 2015.

[32] J.F. Rosenbaum, *Bulk Acoustic Wave Theory and Devices*, Artech House Inc., 1988.

[33] R. P. Paganelli *et al.*, "Modeling and Characterization of Piezoelectric Transducers by Means of Scattering Parameters. Part I: Theory," *Sens. Actuat. A: Phys.*, Vol. 160, pp. 9-18, Mar. 2010.

[34] A. Kasyap, "Development of MEMS-based Piezoelectric Cantilever Arrays for Vibration Energy Harvesting," Ph.D. dissertation, Deptt. Mech. Engg., Univ. Florida, Gainesville, 2006.

[35] A. Phipps, T. Nishida, "System Modeling of Piezoelectric Energy Harvesters," *IEEE Tr. Pwr. Electron.*, Vol 27. No. 2, pp. 790-802, 2012.

[36] H. Xue, Y. Hu, Q.M. Wang, "Broadband Piezoelectric Energy Harvesting Devices Using Multiple Bimorphs with Different Operating Frequencies," *IEEE Trans. Ultrason. Ferr. Freq. Contr.*, Vol-55, No. 9, pp. 2104-2108, Sept. 2008.

[37] B.P. Mann, N.D. Sims, "Energy Harvesting from Nonlinear Oscillations of Magnetic Levitation," *J. Sound Vib.*, Vol. 319, pp. 515-530, 2009.

[38] S.M. Shahruz, "Increasing the Efficiency of Energy Scavengers by Magnets," *J. Comput. & Nonlin. Dyn.*, Vol. 3, 041001 (12 pp.), 2008.

[39] J.-T. Lin, B. Lee, B. Alphenaar, "The Magnetic Coupling of a Piezoelectric Cantilever for Enhanced Energy Harvesting Efficiency," *Smart Mater. Struc.*, Vol. 19, No. 4, 045012 (7 pp.), Apr. 2010.

[40] M. Ferrari *et al.*, "Improved Energy Harvesting from Wideband Vibrations by Nonlinear Piezoelectric Converters," *Sens. Actuat. A: Phys*, Vol. 162, pp. 425-431, May 2010.

[41] R. Ramlan, M.J. Brennan, B.R. Mace, I. Kovacic, “Potential Benefits of a Non-linear Stiffness in an Energy Harvesting Device,” *Nonlinear Dyn.*, Vol. 59, pp. 545-558, 2010.

[42] S.C. Stanton, C.C. McGehee, B.P. Mann, “Nonlinear Dynamics for Broadband Energy Harvesting: Investigation of a Bistable Piezoelectric Inertial Generator,” *Phys. D*, Vol. 239, pp. 640-653, 2010.

[43] F. Cottone, L. Gammaitoni, H. Vocca, “Nonlinear Energy Harvesting,” *Phys. Rev. Lett.*, Vol. 102, 080601, Feb. 2009.

[44] L. Gammaitoni, I. Neri, H. Vocca, “Nonlinear Oscillators for Vibration Energy Harvesting,” *Appl. Phys. Lett.*, Vol. 94, 164102 (3 pp.), 2009.

[45] A.F. Arrieta, P. Hagedorn, A. Erturk, D.J. Inman, “A Piezoelectric Bistable Plate for Nonlinear Broadband Energy Harvesting,” *Appl. Phys. Lett.*, Vol. 97, 104102 (3 pp.), Sept. 2010.

[46] Mathworks Simulink, URL: http://www.mathworks.com/products/simulink/, last accessed Nov. 12, 2015.

[47] Midé Volture Piezoelectric Energy Harvesters Datasheet, Revision 01, Mar. 2010, URL: http://www.mide.com/pdfs/Volture_Datasheet_001.pdf, last accessed Nov. 12, 2015.

[48] G. Ottman, H. Hofmann, A. Bhatt, G. Lesieutre, “Adaptive Piezoelectric Energy Harvesting Circuit for Wireless Remote Power Supply,” *IEEE Trans. Power Electron.*, Vol. 17, No. 5, pp. 669-676, Sep. 2002.

[49] G. Ottman, H. Hofmann, G. Lesieutre, “Optimized Piezoelectric Energy Harvesting Circuit Using Step-Down Converter in Discontinuous Conduction Mode,” *IEEE Trans. Power Electron.*, Vol. 18, No. 2, pp. 696-703, Mar. 2003.

[50] A. Badel *et al.*, “Single Crystals and Nonlinear Process for Outstanding Vibration-Powered Electrical Generators,” *IEEE Trans. Ultrasonics, Ferroel., Freq. Contr.*, Vol. 53, No. 4, pp. 673-684, Apr. 2006.

[51] J. Dicken, P.D. Mitcheson, I. Stoianov, E.M. Yeatman, “Power-Extraction Circuits for Piezoelectric Energy Harvesters in Miniature and Low-Power Applications,” *IEEE Trans. Power Electron.*, Vol. 27, No. 11, pp. 4514-4529, Nov. 2012.

[52] M. Lallart, D. Guyomar, “An Optimized Self-Powered Switching Circuit for Non-Linear Energy Harvesting with Low Voltage Output,” *Smart Mat. Struct.*, Vol. 17, No. 3, p. 035 030, Jun. 2008.

[53] L. Zhu, R. Chen, X. Liu, “Theoretical Analyses of the Electronic Breaker Switching Method for Nonlinear Energy Harvesting Interfaces,” *J. Intell. Mat. Syst. Struc.*, Vol. 23, No. 4, pp. 441-451, Feb. 2012.

[54] L. Zhao, L. Tang, H. Wu, Y. Yang, “Synchronized Charge Extraction for Aeroelastic Energy Harvesting,” *Proc. SPIE 9057: Active & Pass. Smart Struc. & Integ. Syst. 2014*, Vol. 9057, pp. 90570N, Mar. 2014.

[55] H.E. Bass, “The Propagation of Thunder through the Atmosphere,” *J. Acoust. Soc. Am.*, Vol. 67, No. 6, pp. 1959-1966, Jun 1980.

[56] Publication Number: EM 1110-2-1003, Title: Engineering and Design - Hydrographic Surveying Proponent: CECW-EE, CECW-OD, Publication Date: 01 Jan 02, US Army Corp of Engineers, Engineer Manuals, Chapter 21 - Depth Measurement Over Irregular or Unconsolidated Bottoms.

[57] R.J. Weber, Personal communications, ECpE, Iowa State University, Jan. 2012.

[58] V. Agarwal, A. Vishwakarma, "A Comparative Study of PWM Schemes for Grid Connected PV Cell," in *7th Int. Conf. Power Electron. Drive Syst., (PEDS '07)*, pp.1769-1775, 27-30 Nov. 2007.

[59] T. Esram, P.L. Chapman, “Comparison of Photovoltaic Array Maximum Power Point Tracking Techniques,” *IEEE Trans. Energy Conversion*, vol. 22, no. 2, pp. 439-449, Jun. 2007.

[60] A.N.A. Ali, M.H. Saied, M.Z. Mostafa, T.M. Abdel-Moneim, "A Survey of Maximum PPT Techniques of PV Systems," in *IEEE Energytech 2012*, pp.1-17, 29-31 May 2012.

[61] E. Koutroulis, K. Kalaitzakis, “Development of a Microcontroller-based, Photovoltaic Maximum Power Point Tracking Control System,” *IEEE Trans. Power Electronics*, vol. 16, no. 1, Jan. 2001.

[62] E. Koutroulis, K. Kalaitzakis, “Design of a Maximum Power Tracking System for Wind-Energy-Conversion Applications,” *IEEE Trans. Industrial Electronics*, vol. 53, no. 2, pp. 486-494, Apr. 2006.

[63] J. A. Baroudi, V. Dinavahi, A.M. Knight, “A Review of Power Converter Topologies for Wind Generators,” *Renewable Energy*, vol. 32, pp. 2369-2385, 2007.

[64] M. Kesraoui, N. Korichi, A. Belkadi, “Maximum Power Point Tracker of Wind Energy Conversion System,” *Renewable Energy*, vol. 36, no. 10, pp. 2655-2662, Oct. 2011.

[65] A.B. Cultura, Z.M. Salameh, "Modeling and Simulation of a Wind Turbine-Generator System," in *IEEE Power and Energy Society General Meeting, 2011*, pp.1-7, 24-29 July 2011.

[66] Z. Chen, E. Spooner, "Grid Interface Options for Variable-speed, Permanent-magnet Generators," in *Proc. IEE Electric Power Applications*, Vol. 145, No. 4, pp. 273-283, Jul 1998.

[67] Z. Chen, E. Spooner, " Voltage Source Inverters for High-power Variable-voltage DC Power Sources," in *Proc. IEE Generation, Transmission, Distribution*, Vol. 148, No. 5, pp. 439-447, Sep. 2001.

[68] Z. Chen, E. Spooner, "Current Source Thyristor Inverter and Its Active Compensation System," in *Proc. IEE Generation, Transmission, Distribution*, Vol. 150, No. 4, pp. 447-454, July 2003.

[69] Z. Zhi-dan, H. Hai-bo, Z. Xin-jian, C. Guang-yi, R. Yuan, “Adaptive Maximum Power Point Tracking Control of Fuel Cell Power Plants,” *J. Power Sources*, vol. 176, no. 1, pp. 259-269, Jan. 2008.

[70] Y.A. Chang, S.J. Moura, “Air Flow Control in Fuel Cell Systems: An Extremum Seeking Approach,” in *American Control Conf. 2009*, pp. 1052-1059, Jun. 2009.

[71] S. Jain, J. Jiang, X. Huang, S. Stevandic, "Single Stage Power Electronic Interface for a Fuel Cell Based Power Supply System," in *IEEE Electrical Power Conference, 2007, Canada*, pp.201-206, 25-26 Oct. 2007.

[72] M. Tanrioven, M.S. Alam, “Modeling, Control, and Power Quality Evaluation of a PEM Fuel Cell-Based Power Supply System for Residential Use,” *IEEE Trans. Industry Applications*, vol. 42, no. 6, Nov./Dec. 2006.

[73] H.A. Qdais, K.B. Hani, N. Shatnawi, “Modeling and Optimization of Biogas Production from a Waste Digester using Artificial Neural Network and Genetic Algorithm,” *Resources, Conservation, Recycling*, vol. 54, no. 6, pp. 359-363, Apr. 2010.

[74] Z. Yanning, K. Longyun, C. Binggang, H. Chung-Neng, W. Guohong, “Renewable Energy Distributed Power System with Wind Power and Biogas Generator,” in *Transmission Distribution Conf. Expo.: Asia Pacific 2009*, pp.1-6, 26-30 Oct. 2009.

[75] D. Zhu, S.P. Beeby, “Scaling Effects for Piezoelectric Energy Harvesters,” in *Proc. SPIE 9517, Smart Sensors, Actuators, and MEMS VII; and Cyber Physical Systems*, pp. 95170P-1 – 95170P-9, May 2015.

APPENDIX

COMPONENTS AND INSTRUMENTS USED

Table A 1 lists the components used in the prototype and the extraction circuits, while Table A 2 lists the instruments used in the experimental setup.

Table A 1: Components used in the experimental setup.

Component	Component ID	Manufacturer/Supplier
Piezoelectric cantilever	Volture V21B	Midé
Magnets	D48	K&J Magnetics
Electromagnet ferrite core	2673021801	Fair-Rite Products Corp.
Diodes	1N4148	Digi-Key
Transformer	DA103C	Digi-Key
PNP Transistors	Q2N2907A	Digi-Key
NPN Transistors	Q2N3904	Digi-Key
Resistors, Capacitors, Inductors	-	Digi-Key

Table A 2: Instruments used in the experimental setup.

Instrument	Manufacturer and Model
Function generator	Tektronix AFG 3021B
DC Power supply	Agilent E3631A
Digital oscilloscope	Agilent DSO-X 2024A
Multimeter	Keysight 34410A